JOURNAL OF GEOPHYSICAL RESEARCH, VOL. 104, NO. B5, PAGES 10,841–10,861, MAY 10, 1999

Continuous near-bottom gravity measurements made with a BGM-3 gravimeter in DSV *Alvin* on the East Pacific Rise crest near 9°31'N and 9°50'N

James R. Cochran,[1] Daniel J. Fornari,[2] Bernard J. Coakley,[1]
Randall Herr,[3] and Maurice A. Tivey[2]

Abstract. A Bell BGM-3 gravimeter has been used to collect continuous, underway, near-bottom (3- to 10-m altitude) gravity measurements from the deep-diving submersible DSV *Alvin* during surveys on the East Pacific Rise (EPR) crest near 9°31'N and 9°50'N. Closely spaced (20- to 30-m) gravity measurements were made along transects up to 8 km long in both regions. Repeatability of measurements made at the same location on different dives is ~0.3 mGal. Along-track spatial resolution of anomalies is ~130-160 m, with the limiting factors being precision and sampling rate of the pressure gauge depth data used to calculate vertical accelerations of the submersible. The average upper crustal density of the ridge crest determined from the relationship between depth and free-water gravity anomalies varies greatly between 9°31'N and 9°50'N. Average upper crustal densities of 2410 kg/m^3 for the 9°50'N area and 2690 kg/m^3 for the 9° 31'N area were calculated. The different densities are not due to differing geometry of the Layer 2A-2B boundary or a regional cross-axis gravity gradient. Differences in porosity of the shallow crustal rocks, or a difference in the proportion of low density extrusives to higher-density dikes and sills within Layer 2A in these two areas, are the likely causes of the different upper crustal densities. Bouguer gravity anomalies near the EPR axis are primarily small amplitude (0.5-2 mGal), are a few hundred meters across, and appear to be lineated parallel to the axis. Larger-amplitude Bouguer anomalies of up to 4 mGal were found at a few locations across the crestal plateau and are associated with pillow ridges composed of lavas which are clearly younger than the surrounding seafloor. These ridges have distinct chemical compositions compared to lavas from the axial summit collapse trough (ASCT) at the same latitude. Probable sources of the 0.5- to 2-mGal anomalies observed on the summit plateau include areas of collapsed and fissured terrain and dike swarms feeding melt through Layer 2A to the surface. A grid survey of the ridge axis near 9°50'N shows Bouguer anomalies lineated along the axis, suggesting that dike swarms do contribute to the observed Bouguer anomalies. The along-axis continuity of the gravity anomalies is disrupted at a 75-m offset of the ASCT, suggesting that shallow feeders of lava to the surface may be segmented on a finer scale than the deeper crustal magmatic system. This initial study confirms the ability to conduct high-resolution, near-bottom, continuous gravity measurements from *Alvin*. It also provides important information on how the shallow crustal structure of a fast spreading mid-ocean ridge develops and how it varies with the surface morphology.

1. Introduction

Marine gravity measurements have been made from surface ships for 40 years [*Worzel*, 1959] and have been widely used to investigate the gross crustal structure and isostasy throughout the oceans. Surface ship gravity measurements are, however, limited in resolution by the several kilometers of water between the measurement site and source of the gravity anomalies. As a result, marine gravity studies have focused on anomalies with wavelengths >5-10 km. These wavelengths can be used to address questions such as crustal thickness variations, mantle density variations, and isostatic compensation. Gravity studies have not yet proved useful for detailed studies of the shallow structure of oceanic crust, largely because surface measurements lack the necessary resolution.

Seafloor gravity measurements have been made using LaCoste land gravimeters, either within a submersible [*Luyendyk*, 1984] or lowered from a surface ship in a pressure case [*Hildebrand et al.*, 1990]. These techniques produced on-bottom gravity measurements estimated to be accurate to within 0.5 mGal. However, both methods are very time-consuming, resulting in only about 10-20 measurements per day, which severely limits both the areal coverage and the resolution of the resulting survey. In addition, the location of measurements made with the over-the-side system is known only to within 100-200 m because of uncertainties in estimating the wire angle and the on-bottom position of the instrument [*Stevenson et al.*, 1994]. Measurements made using the over-

---

[1] Lamont Doherty Earth Observatory of Columbia University, Palisades, New York.

[2] Department of Geology & Geophysics, Woods Hole Oceanographic Institution, Woods Hole, Massachusetts.

[3] Naval Oceanographic Office, Stennis Space Facility Center, Mississippi.

Paper number 1999JB900049.
0148-0227/99/1999JB900049$09.00

the-side instrument [*Hildebrand et al.*, 1990; *Stevenson et al.*, 1994; *Stevenson and Hildebrand*, 1996] or within a submersible sitting on the seafloor [*Luyendyk*, 1984; *Holmes and Johnson*, 1993; *Evans*, 1996] have provided useful estimates of average upper crustal density, but the uncertainties in location (for surface-deployed instruments) and limitations on the number of measurements which can be made using these techniques limit their utility for investigation of detailed crustal structure at the scale required to map zones of volcanic intrusion, hydrothermal deposits, or regions of alteration or low porosity in the shallow ocean crust.

Another method to make near-source gravity measurements is the TOWDOG system [*Zumberge et al.*,1997], which can be towed above the seafloor. Tests of this system off the coast of California showed a repeatability of a few tenths of a mGal [*Zumberge et al.*, 1997]. TOWDOG allows closely spaced gravity measurements to be made at an elevation of 30 - 50 m above the seafloor. The main limitations of this system are that it must be towed at a safe distance (30-50 m) above the seafloor, that its maneuverability is limited, and that no visual observations are made of the seafloor to link the gravity to local geologic structures.

These restrictions can be overcome by making underway gravity measurements within a submersible. This paper describes the acquisition, reduction, and interpretation of the first continuous, underway near-bottom gravity measurements made with a Bell BGM-3 gravimeter mounted in the personnel sphere of the submersible *Alvin*. A series of dives on the East Pacific Rise (EPR) crest near 9°31'N and 9°50'N (Figure 1) collected densely sampled (20- to 30-m spacing) gravity and bathymetry measurements along profiles up to 8 km long and demonstrated the reliability of these measurements. The gravity data collected from *Alvin* can be combined with other near-bottom geological and geophysical observations to investigate the density distribution and structure within the upper crust. Advantages of a submersible for underway near-bottom gravity surveys include the fact that observations are made close to the seafloor (<10 m) along a well-navigated track and visual observations are made simultaneously with other geophysical measurements. This allows very high resolution investigation of the shallow crustal structure (Figure 2) and correlation to the bottom morphology and geologic features.

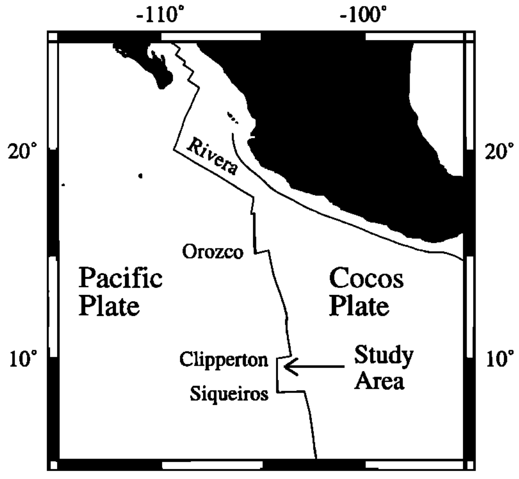

Figure 1. Map showing the location of the field area with respect to plate boundaries and North America. Major transforms are also identified. Within the study area, detailed surveys were undertaken near 9°31'N and 9°50'N.

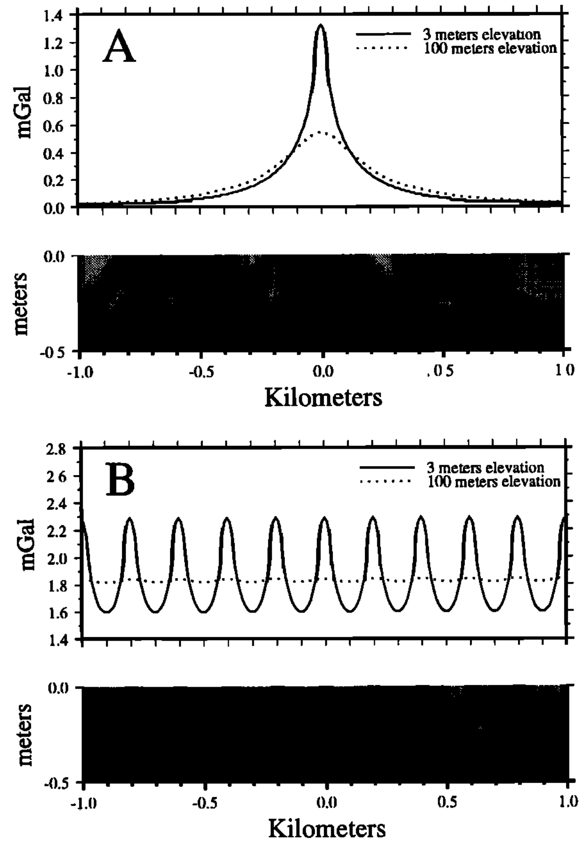

Figure 2. Gravity models showing the effects of distance from the source on observed gravity anomalies. a) Gravity anomalies resulting from a 50-m-wide vertical-sided zone of dike intrusion with a density contrast of 600 kg/m^3 with the surrounding rocks. The density contrast is assumed to extend to a depth of 300 m below the seafloor. Calculated gravity anomalies are shown measured at heights of 3 m and 100 m above the seafloor. b) Gravity anomalies resulting from a series of 50-m-wide vertical-sided dike swarms located 200 m apart. The density contrast of 600 kg/m^3 is assumed to extend to a depth of 300 m below the seafloor. Calculated gravity anomalies are shown measured at heights of 3 m and 100 m above the seafloor.

2. Why Measure Gravity Near the Seafloor?

The water column effectively acts as a low-pass filter, which results in a loss of detail and of spatial resolution in gravity measurements collected at the sea surface. The gravity anomaly resulting from a two-dimensional feature of wavelength λ falls off with distance above the source by a factor of $e^{-2\pi z/\lambda}$ equivalent to multiplication of the anomaly by e^{-kz} in the wavenumber domain), where z is the vertical coordinate, λ is the wavelength, and k is the wavenumber. Thus, not only is amplitude attenuated with increased distance from a source, but short-wavelength (high-wavenumber) components are preferentially attenuated.

The effects of increasing distance from a source in the upper oceanic crust can be seen in Figure 2. Figure 2a shows the anomalies resulting from a 50-m-wide two-dimensional vertical intrusion with a density contrast of 600 kg/m^3 with the surrounding rock extending to a depth of 300 m below the seafloor. This body could, for example, be a zone of concentrated dike intrusion into crustal Layer 2A. The solid line shows the anomalies which would be recorded while traversing the body at an altitude of 3 m off the seafloor. The dotted line shows the anomalies measured on a traverse at an altitude of 100 m. The maximum gravity anomaly amplitude is reduced by a factor of 2.4, from 1.32 to 0.55 mGal, by simply moving 100 m off the seafloor. If the measurements are made at an altitude of 1 km, the anomaly amplitude is reduced to <0.1 mGal, below the noise level of most marine gravity systems. The effect of distance from the source is even more pronounced when there are several sources whose gravity effects are superimposed. Figure 2b shows the gravity anomalies resulting from a series of 50-m-wide bodies identical to that in Figure 2a, spaced at 200 m intervals. The resulting gravity anomalies have an amplitude of 0.7 mGal when observed at 3 m altitude but are reduced to 0.02 mGal at 100 m. Clearly, gravity studies of shallow crustal structure require near-source surveys.

3. Instrumentation and Installation in *Alvin* and Data Acquisition

The Bell Aerospace BGM-3 gravimeter is commonly used for surface-ship marine surveys and is described by *Bell and Watts* [1986]. The meter was installed in *Alvin*'s personnel sphere, taking care to isolate the various electrical components from the submersible hull and to insure that uninterrupted power could be provided to the meter at all times.

Navigation for the dives relied on three bottom-moored transponders oriented along an east-west line ~1.5 km south of the intended submersible traverses in each dive area (Figures 3 and 4). For dive 2770 navigation we used an existing net of nonrecoverable transponders used for navigation in the Biological-Geological Transect, a time-series experiment located along a 1.3-km-long portion of the EPR crest between 9°49.6'N and 9°50.3'N [*Shank et al.*, 1994; 1998]. Occasional navigation dropouts between *Alvin* and the transponders required interpolation of positions along short portions of a few dive tracks.

In order to assess the repeatability of underway gravity measurements, we placed benchmarks, numbered bucket lids (G1 - G17) with large scrap chain anchors, at fixed points on the seafloor along east-west oriented traverses (Figures 3 and 4). During the initial dive in each area we deployed the markers and sat at each site for 10-15 min after the meter had stabilized (average stabilization time was 3-5 min). On subsequent dives we continuously traversed the seafloor at average speeds of ~1.0 knots within visual and photographic range of the bottom (3-7 m). Continuous gravity data were collected on each dive of the field program, both while traversing between fixed gravity stations on the seafloor and on dives where traverses were largely uninterrupted. Speed and altitude above the seafloor were kept as constant as possible on traverses across

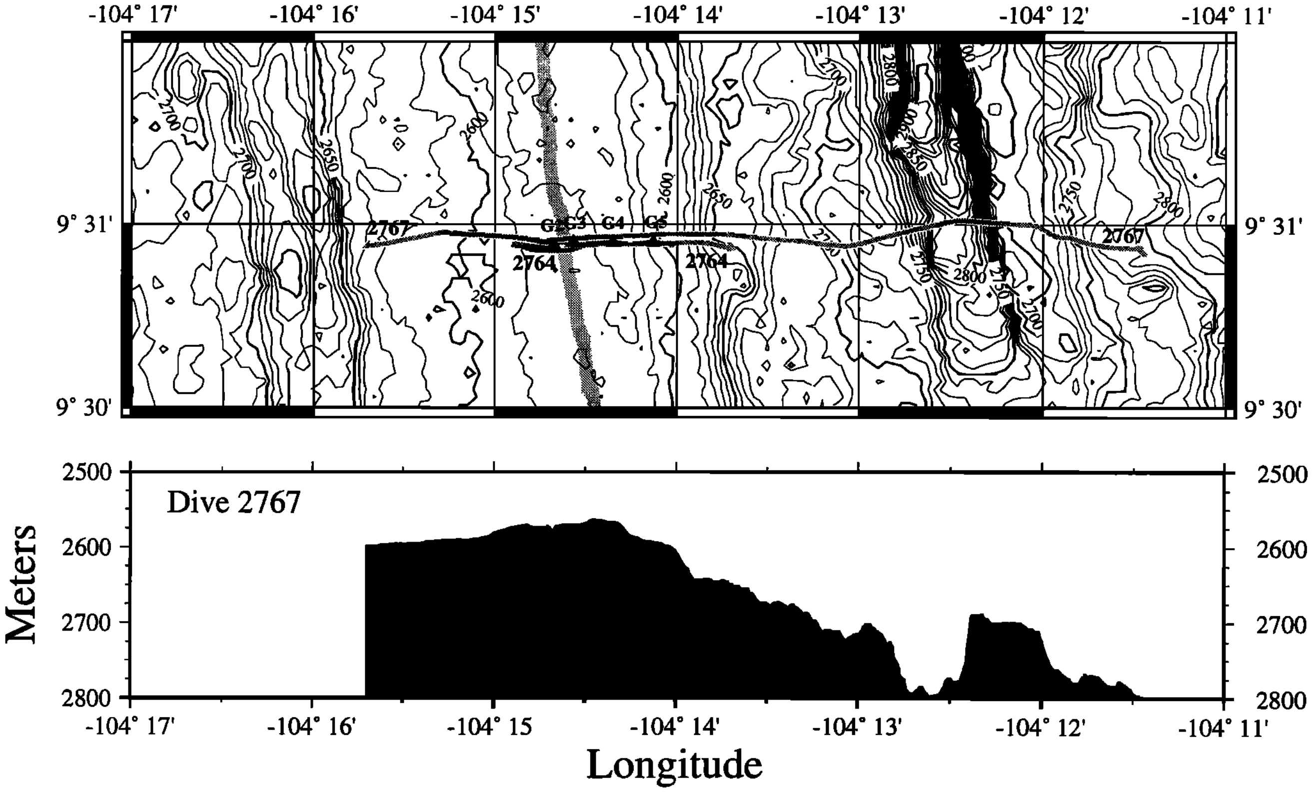

Figure 3. Bathymetry of the southern dive sites near 9°31'N. The top diagram shows a SeaBeam bathymetry map of the 9°31'N area contoured at 10-m intervals and *Alvin* tracks for the gravity traverses obtained on Dives 2764 and 2767. Location of the axial summit collapse trough (ASCT) from *Fornari et al.* [1990, 1998] is shown in gray. Triangles show the locations of fixed bottom gravity sites G2-G5. The bottom diagram shows the bathymetric profile obtained during Dive 2767.

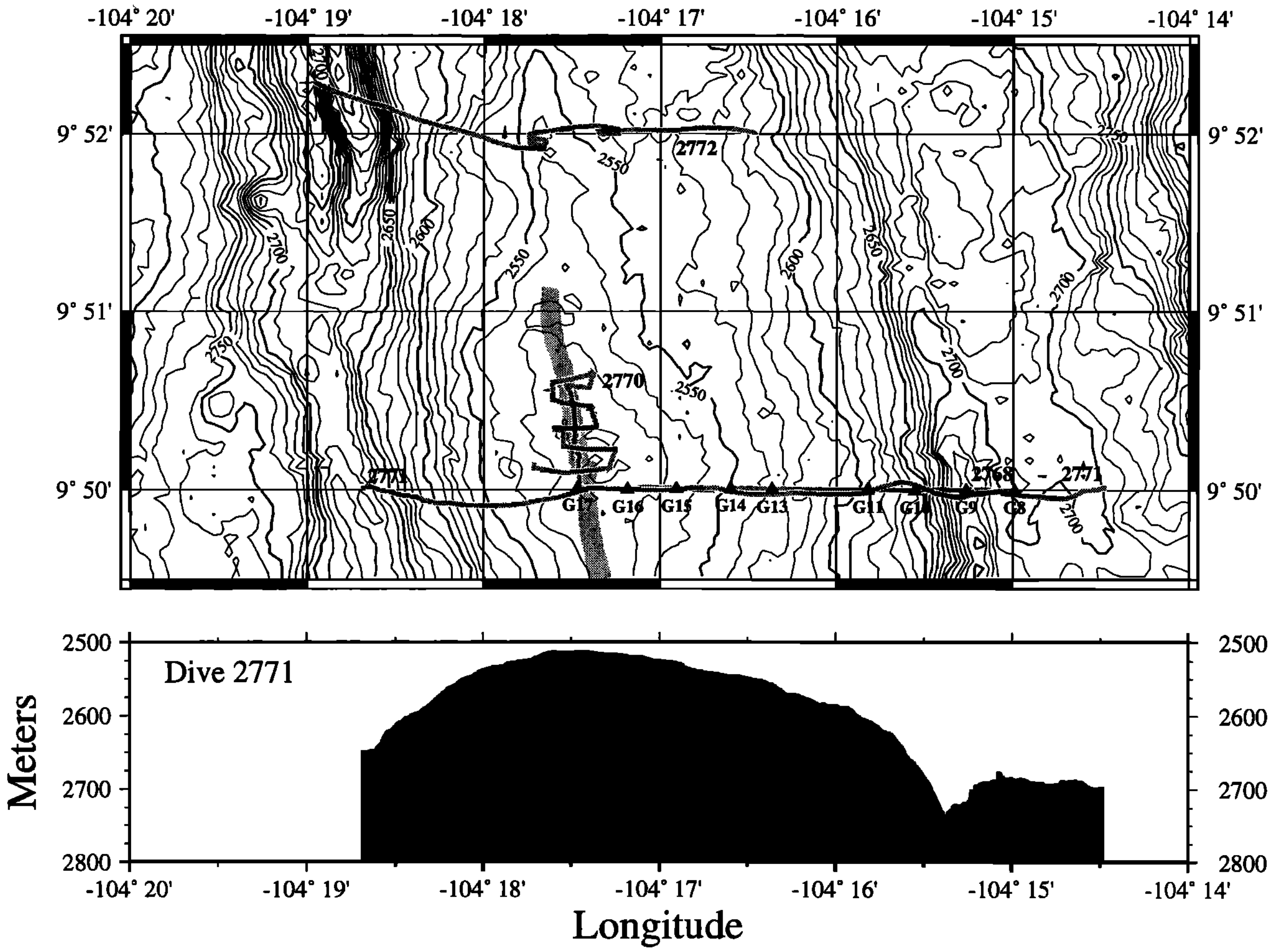

Figure 4. Bathymetry of the northern dive sites near 9°50'N. The top diagram shows a SeaBeam bathymetry map of the 9°50'N-9°52'N area contoured at 10 m intervals and *Alvin* tracks for Dives 2768, 2770, 2771, and 2772. Location of the ASCT from *Fornari et al.* [1990, 1998] is shown in gray. Triangles show the locations of fixed bottom gravity sites G8-G17. The bottom diagram shows the bathymetric profile obtained during Dive 2771.

the seafloor. Continuous near-bottom magnetic measurements were also acquired using *Alvin*'s three-axis fluxgate magnetometer [*Tivey*, 1996; *Schouten et al.*, 1999].

4. Data Processing

The 1-Hz output of a BGM-3 gravimeter must be low-pass filtered to produce a coherent signal. A 120- to 240-sec Gaussian filter is widely used for this purpose. The gravimeter output is the sum of the gravitational acceleration and any other vertical accelerations experienced by the meter. Surface ship vertical accelerations can be very large, but average to zero over the characteristic period of the wave motions (10-30 s), so the effects of ship motions are removed by the filtering [*Bell and Watts*, 1986]. However, a submersible has no imposed constraints to its motions. Vertical accelerations are not constrained to average to zero over any particular time interval. Vertical accelerations due to *Alvin*'s vertical motions (Figure 5f) must be calculated and explicitly subtracted from the measurements.

Vertical accelerations were determined by numerically calculating the second derivative of pressure gauge depth data (Figure 5e). The numerically determined accelerations were passed through the same 180-s Gaussian filter applied to the raw meter output (Figure 5d). The raw gravity signal (Figure 5c) was determined by subtracting the submersible's vertical accelerations from the meter output. The raw gravity values were corrected for effects of variations in submersible depth (free-water correction), shape of the Earth (latitude correction), and the fact that measurements were made from a moving platform on a rotating Earth (Eötvös correction), to produce free-water gravity anomalies (Figure 5b). The free-water correction differs from the free-air correction in that it accounts not only for the difference in elevation between two observations, but also for the gravitational attraction of the slab of seawater between the two observation depths. As a result, the vertical gravity gradient in seawater is taken as 0.22242 mGal/m rather than the value of 0.3086 mGal/m commonly used for the free-air correction.

The spatial resolution of the gravity data was limited by the necessity to filter out short-period (75- to 150-s) noise in the free-water anomalies (Figure 5b). These variations cannot be of geologic origin since implausibly large density contrasts (>1000 kg/m^3) are required to reproduce the amplitude and

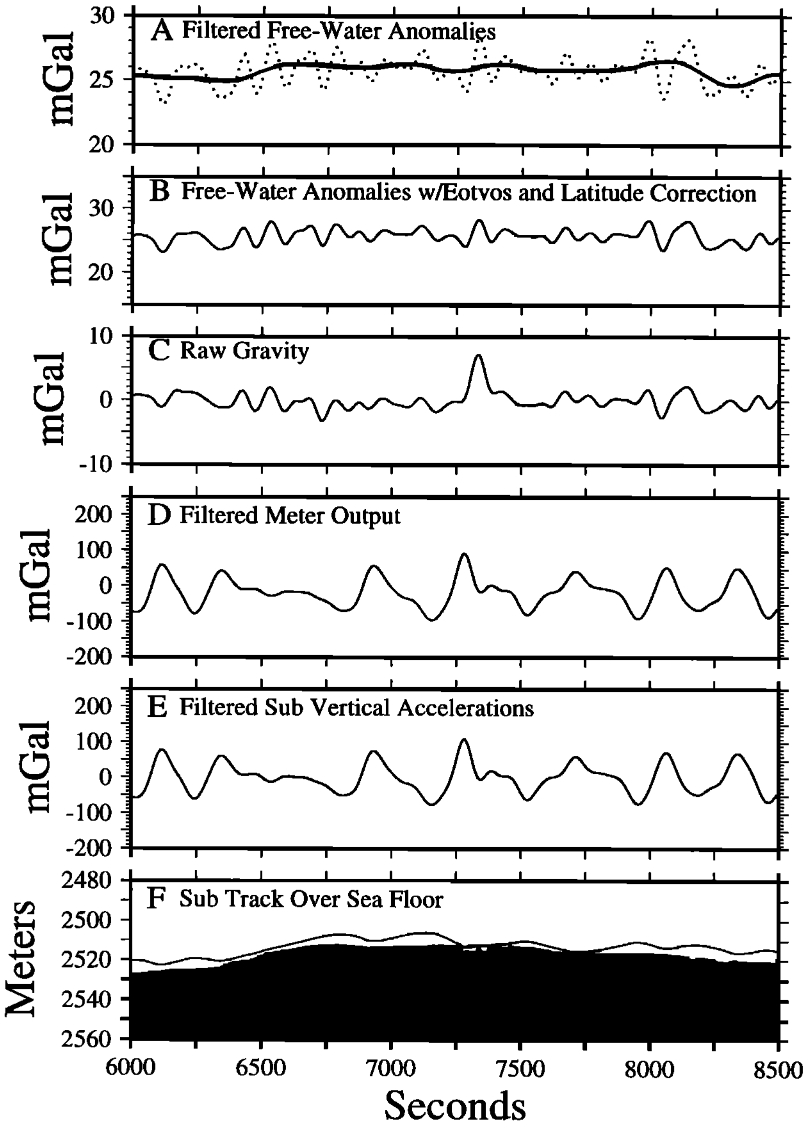

Figure 5. Gravity data processing steps. (f) *Alvin* track above the seafloor during a 2500-s (41.7-min) portion of Dive 2771 (The total length of the profile shown is 1322 m.), (e) vertical accelerations experienced by *Alvin* calculated from the second derivative of the pressure gauge depth data passed through a 180-s Gaussian filter, (d) meter output passed through a 180-s Gaussian filter, (c) raw gravity data obtained by subtracting *Alvin*'s vertical accelerations from the meter output (Mean value has been removed from data for display; note change in vertical scale between Figures 5d and 5c.), (b) gravity data corrected for variations in submersible depth (free-water correction) and with application of latitude and Eötvos corrections, and (a) free-water gravity anomalies after application of a Parks-McClellan low pass-filter (solid line); dotted line shows unfiltered data. The filtering effectively removes the high frequency noise but limits spatial resolution to 130-160 m. Note change in vertical scale between Figures 5b and 5a.

short wavelength (30-80 m) of the anomalies. We were able to filter this noise from the data using a Parks-McClellan low-pass filter, which effectively removed periods of less than about 270 sec, while the longer period signal remained unaffected. Both the filtered and unfiltered free-water anomalies are illustrated in Figure 5a.

Since signal and noise cannot be clearly separated on the basis of frequency (Figure 6), we applied a series of filters with successively longer wavelength cutoffs. The criterion used to determine the filter finally adopted was that quasiperiodic variations with wavelengths too short to be geologically possible were not visually apparent in the data. This is a subjective decision and it is almost certain both that some shorter-wavelength anomalies have been removed and that some longer-wavelength noise is still present. Figure 7 shows the effects of filtering on the data by comparing the final filtered gravity anomalies for the Dive 2764 profile across the axis with the unfiltered gravity data from the same profile and with those data filtered using a different filter having a shorter wavelength cutoff. The anomalies present in the final data are also present at the same location in the two other data sets, demonstrating that the pattern and spacing of anomalies is not simply a result of the filtering process.

We are also confident that the anomalies in the filtered

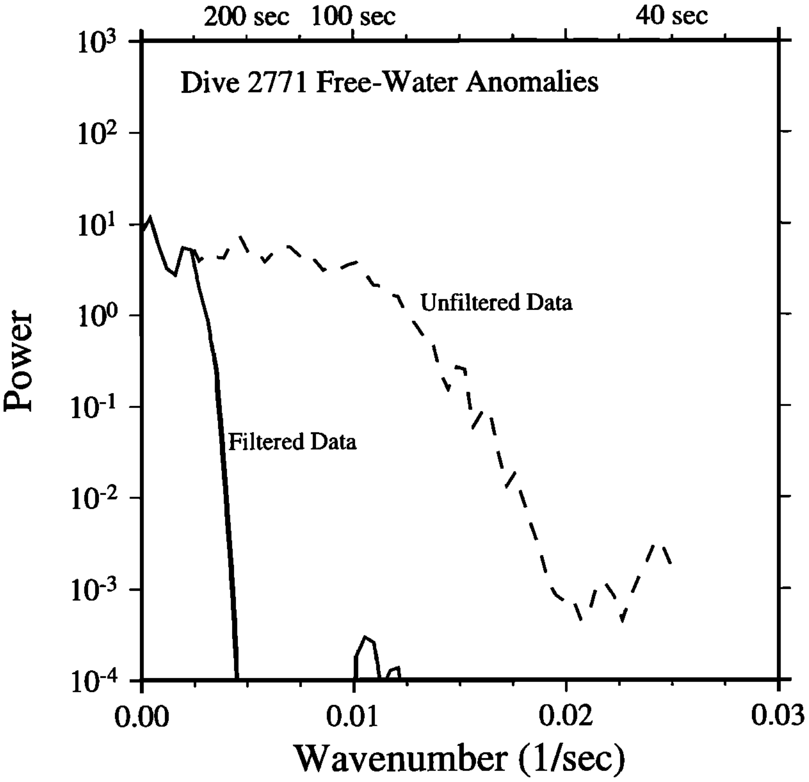

Figure 6. Power spectra of unfiltered free-water anomalies (dashed line) and of low-pass filtered free-water anomalies for Dive 2771. The filter removes signals with periods shorter than about 270 s while the longer period signal remains unaffected.

gravity data are of geologic origin. This is demonstrated in Figure 8, which compares the free-water anomalies measured across the ridge axis during Dives 2764 and 2767. These two profiles were run during two different dives in opposite directions on parallel lines separated by about 100 m (Figure 3). Although the amplitudes of individual anomalies vary between the two profiles reflecting along-strike variation in the sources and any residual noise, the same pattern of anomalies is observed, confirming that the anomalies are of geological origin and not artifacts introduced by the data processing and filtering. This is further demonstrated by the observation that during the grid survey of the ridge axis carried out on Dive 2770 (Figure 4), a coherent and mappable pattern of anomalies was observed for over 1 km along the axis (see Figures 16a and 16b).

Filtering limits our resolution to gravity signals with periods >270 s (Figure 6). The gravity transects were carried out at a speed of 0.5 - 0.6 m/s (~1.0 - 1.2 knots), so gravity anomalies with wavelengths greater than ~135-165 m can be resolved in our data. Since gravity anomalies are wider than their source (see Figure 2), narrower bodies can be detected, particularly if they extend to depth of a few hundred meters or more into the crust.

We have identified the source of this noise as the limited sampling rate and precision of the submersible's pressure depth data. In 1994, the *Alvin* data logger recorded submersible depth measurements at 2-s intervals with 10-cm resolution, even though the pressure depth transducer then on *Alvin* was capable of resolving 1-cm depth variations at 1-s intervals.

We investigated the effect of the limited resolution of *Alvin* depth data on the calculation of the vertical accelerations using synthetic submersible tracks. In the first experiment (Figure 9), the vertical component of the submersible track was defined by a sinusoidal function which allowed the vertical accelerations to be analytically calculated. The synthetic track was sampled at 2-s intervals with a resolution of 10 cm, and at 1-s intervals with a resolution of 1 cm. Vertical accelerations were determined numerically from these two data sets in the same manner as for the actual submersible data. Maximum differences from the analytic solution were < ±0.07 mGal for the 1-s, 1-cm data, but of the order of ±1.2 mGal for the 2-s, 10-cm data. The noise in the 2-sec, 10-cm data was similar in appearance to, but of lower amplitude, than, noise in the real data. This may be because the synthetic submersible track was smoother than the actual submersible track. A more realistic example was defined by fitting a spline through the recorded depths for a portion of dive 2771 and sampling it at 1-s intervals with 1-cm resolution, and at 2-s intervals with 10-cm resolution (Figure 10). In this exercise the difference between accelerations determined from 1-cm data and accelerations determined from the 10-cm data approximates the noise introduced into gravity anomalies by truncation of depth data. This noise has an amplitude of ±3 mGal and is similar in appearance to the noise observed in the *Alvin* data (Figure 5b). Changes subsequently implemented in the *Alvin* data logging system (1-Hz recording of all attitude data and greater precision in logging the pressure gauge depth) will remove the source of this noise, drastically reducing or eliminating the need for extensive filtering of the data and will thus greatly improve the spatial resolution of measurements during future surveys.

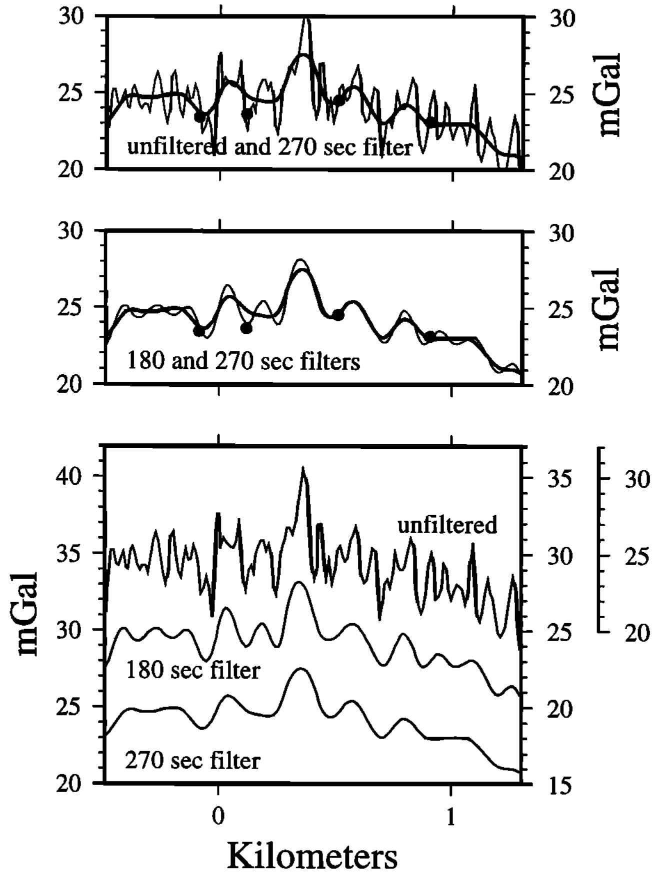

Figure 7. Effects of filtering on free-water anomalies. The bottom plot shows the unfiltered free-water anomalies for a profile across the ridge axis from Dive 2764 along with two profiles of that data after filtering with Parks-McClellan filters which pass wavelengths longer than 180 s and longer than 270 s. The 270-s filter was that used to produce the final filtered data shown in subsequent figures. The profiles are offset by 5 mGal. The top and middle plots show the final data overlain on the unfiltered data and data filtered with the 180-s filter. In both cases the final data is the thicker curve. The solid black dots are the free-water gravity anomalies obtained at markers G2-G5 (Figure 3) while *Alvin* was sitting motionless on the bottom.

5. Field Area: East Pacific Rise 9°30'N - 9°52'N

We chose the axis and summit plateau of the fast spreading (110 mm/yr full rate) [*Carbotte and Macdonald*, 1992] EPR in the region from 9°30'N to 9°52'N (Figure 1) as the field area for our study. The 9°N-10°N segment of the EPR extends for ~130 km from an 8 km offset overlapping spreading center (OSC) at 9°03'N to the Clipperton transform at 10°10'N. The segment is magmatically active. A continuous axial magma lens reflector is observed from the 9°03'N OSC to within 2 km of the Clipperton transform [*Detrick et al.*, 1987; *Barth et al.*, 1994]. The axial topographic high is generally broad with a large cross-sectional area [*Scheirer and Macdonald*, 1993] and a rectangular or domal summit [*Macdonald and Fox*, 1988]. Argo I studies showed abundant evidence of recent volcanism and hydrothermal activity with at least 45 active high-temperature sites [*Haymon et al.*, 1991]. Volcanic eruptions in 1991 and 1992 have been documented between ~9°45'N and 9°51'N [*Haymon et al.*, 1993; *Rubin et al.*, 1994], near the shallowest portion of the segment.

Multichannel seismic reflection studies of the 9°N-10°N area have identified a strong, nearly continuous reflector at a depth of 0.1-0.3 s beneath the seafloor reflector [*Harding et al.*, 1993; *Vera and Diebold*, 1994], which is interpreted as arising from the base of crustal Layer 2A. Comparisons with ophiolites [*Kidd*, 1977; *Gass*, 1989] suggest that Layer 2A is made up primarily of extrusive lava flows, while Layer 2B, underlying it, consists of sheeted dikes. *Christeson et al.* [1992, 1994, 1996] used high-resolution on-bottom seismic refraction experiments to study the shallow crustal structure in the immediate vicinity of the EPR axis at 9°30'N. They found Layer 2A to consist of a "surficial low-velocity layer" with seismic velocity $V_p < 2.5$ km/s, separated by a high-gradient region from a layer with $V_p = 4.25 - 4.35$ km/s, which, in turn, is separated by another high-gradient region from Layer 2B with V_p of ~5.0 km/s.

An axial summit collapse trough (ASCT) [*Fornari et al.*, 1998] is present along most of this portion of the EPR crest. The ASCT varies in width from ~40 m near 9°50'N to ~300 m near 9°33'N. North of 9°51'N, no well-defined trough is present, and the axial zone is characterized by one or several en echelon ~5- to 20-m-wide fissures [*Haymon et al.*, 1991; *Wright et al.*, 1995; *Fornari et al.*, 1998]. The ASCT is the locus of most volcanic and hydrothermal processes occurring on the ridge segment [*Haymon et al.*, 1991, 1993; *Haymon*, 1996].

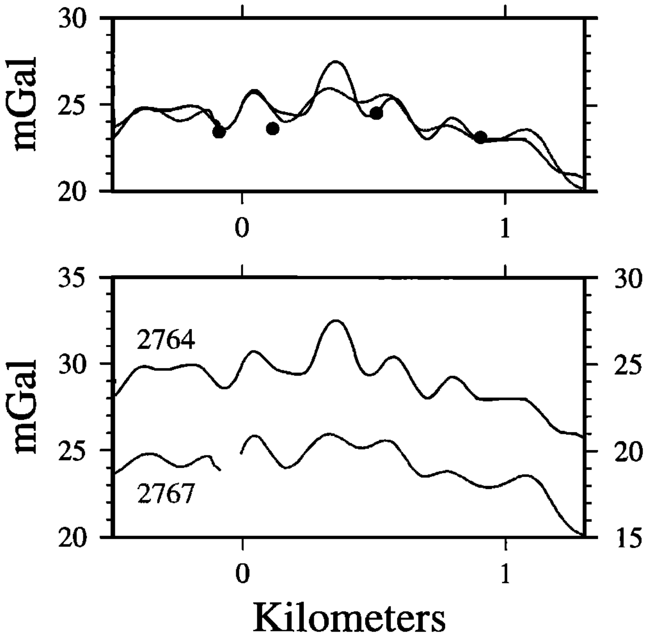

Figure 8. Comparison of the free-water gravity anomaly profiles across the ridge axis from Dives 2764 and 2767 (Figure 10a). These two profiles were collected on parallel lines separated by about 100 m (Figure 3) and run in opposite directions. The profiles are offset by 5 mGal on the lower plot. The top plot shows the two profiles superimposed. Although the amplitudes of individual anomalies vary between the two profiles, the same pattern of anomalies is observed, confirming that the anomalies are of geological origin and not artifacts introduced by the data processing and filtering.

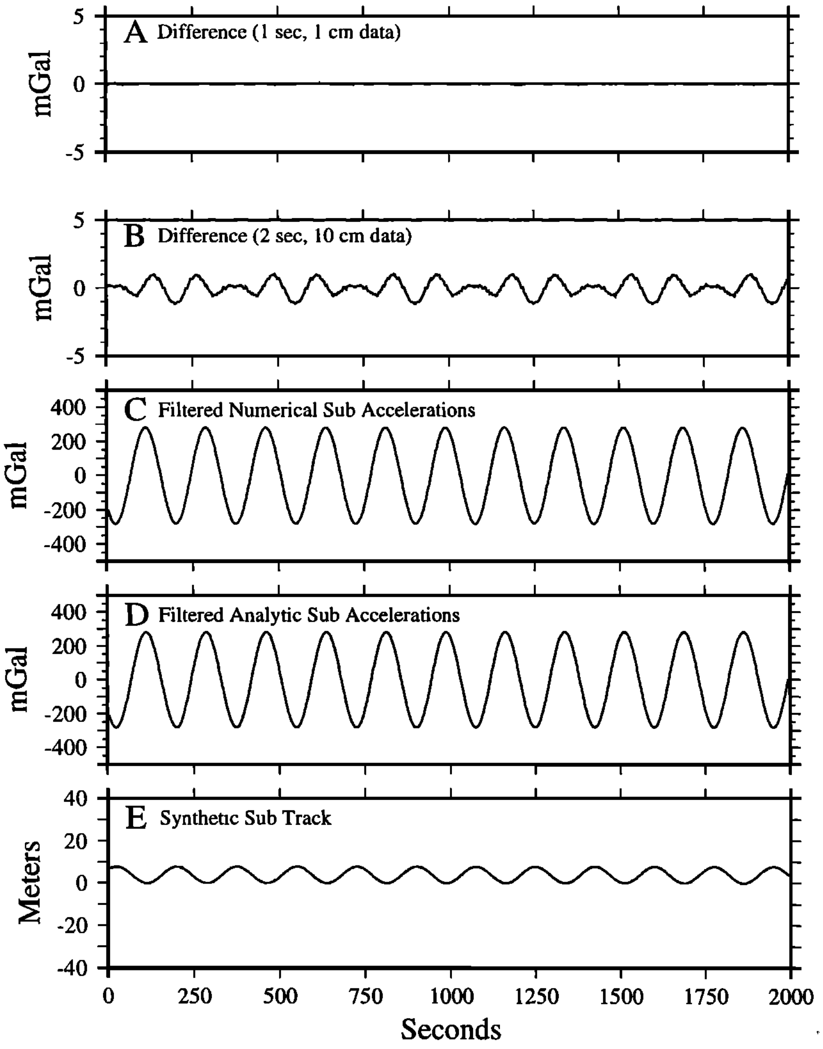

Figure 9. Example of how noise can be introduced into gravity data by limitations in recording submersible depth data. This example assumes a sinusoidal track. (e) Synthetic submersible track, (d) vertical accelerations calculated analytically as the second derivative of the synthetic submersible track shown in Figure 9e, (c) vertical accelerations determined numerically from the synthetic submersible track shown in Figure 9e sampled at 2-s intervals with 10-cm resolution and at 1-s intervals with 1-cm resolution. (The two curves are on top of each other at this scale.), (b) difference between the analytically determined accelerations and the accelerations determined numerically using the data sampled at 2-s intervals with 10-cm resolution (noise), and (a) difference between the analytically determined accelerations and the accelerations determined numerically using the data sampled at 1-s intervals with 1-cm resolution (noise). Note that more precise and rapid sampling of depth data, now possible in *Alvin*, almost completely eliminates this source of noise.

Over distances of >10 km the ASCT is sinuous in map view. On the basis of observations of the seafloor, this sinuosity arises from irregular surface collapse of the ASCT walls [*Fornari et al.*, 1998]. Distinct changes in trough width occur principally at Devals. At these small fourth-order offsets the axial trough is discontinuous for short distances (<2 km) and/or its azimuth changes along small kinks and bends or short (<0.5- to 1-km) lateral en echelon steps [*Langmuir et al.*, 1986; *Macdonald et al.*, 1988; *Haymon et al.*, 1991]. Where the trough is wide, the walls are more linear and tectonic in character on the basis of Argo I sonar and observations from *Alvin*.

Our gravity traverses were situated over the EPR crestal plateau and upper flanks in two areas of contrasting axial morphology. At 9°31'N (Figure 3) the ASCT is ~250 m wide, both high- and low-temperature hydrothermal activity is present but not extensive [*Haymon et al.*, 1991], and dive transects east and west of the ASCT in this area indicate that extensive volcanism has occurred outside the ASCT [*Perfit et al.*, 1994] . At the second area, from 9°50'N to 9°52'N (Figure 4), the ASCT is only 40 m to 70 m wide, with extensive areas of high-temperature hydrothermal venting [*Von Damm et al.*, 1995]. This is the area which experienced an eruption in April 1991 [*Haymon et al.*, 1993].

Dive tracks in each region are shown superimposed on SeaBeam bathymetry in Figures 3 and 4. During the initial dives in each region, we deployed weighted markers at fixed points on the seafloor along traverses across the summit plateau. After deploying each marker, gravity data was collected while *Alvin* sat motionless on the seafloor for 10-15 minutes in or-

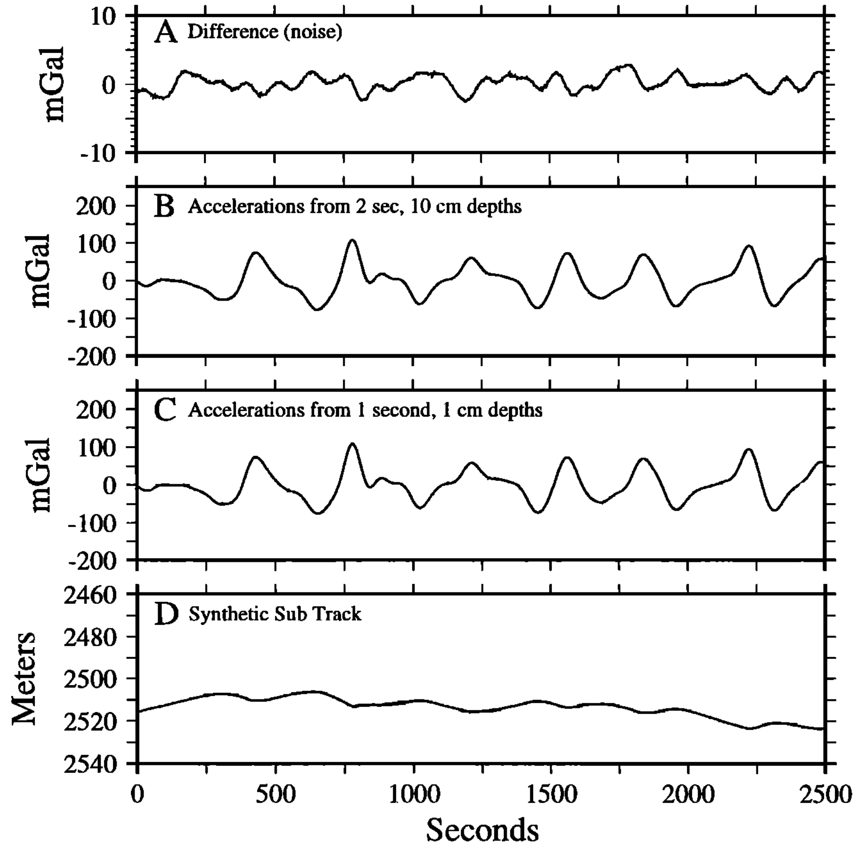

Figure 10. Example of how noise can be introduced into gravity data by limitations in recording submersible depth data. This example assumes a synthetic submersible track determined by fitting a spline curve through observed submersible depths for a 2500-s segment of Dive 2771: (d) Synthetic submersible track, (c) vertical accelerations calculated numerically from the submersible track in Figure 10d sampled at 1-s intervals with 1-cm resolution, (b) vertical accelerations calculated numerically from the submersible track in Figure 10d sampled at 2-s intervals with 10-cm resolution, and (a) difference between vertical accelerations calculated from 1-s, 1-cm data and from 2-s, 10-cm data (noise). The noise introduced by less precise sampling of the depth data very closely resembles that present in the unfiltered observed data (Figure 5b).

der to establish a gravity station. On a subsequent dive we ran a continuous traverse across the markers at a speed of 0.75 - 1.0 knot (23 - 31 m/min). In the 9°50'N area we also conducted a grid survey of the axial trough between 9°50'N and 9°51'N in the region of the 1991 eruption and ran an additional traverse across the summit plateau near 9°52'N in a region which lacks a well-defined axial trough according to Argo I sonar data [*Fornari et al.*, 1990, 1998; *Haymon et al.*, 1991] (Figure 4).

6. Free-Water Gravity Anomalies

Bathymetry and free-water anomaly profiles for the four across-axis traverses are shown in Figures 11a and 11b. Locations of the traverses are shown in Figures 3 and 4. Free-water gravity values recorded during stationary bottom measurements at the bottom gravity markers are also shown in Figures 11a and 11b. Reliable gravity measurements were obtained at 13 of the 17 bottom stations. At the other four stations, bottom measurements were not usable either because *Alvin* was shielded from the transponders while sitting on the bottom, preventing accurate location of the station, or because the submersible shifted while on the bottom so that a reliable gravity value was not obtained. A comparison of the stationary measurements and nearest fly-over value for each gravity traverse is shown in Figure 12. There are four fly-over comparisons with fixed gravity marker measurements for each of the two southern traverses (Dives 2764 and 2767), and nine comparisons for the northern Dive 2771 traverse.

The extent to which fixed measurements confirm underway measurements made from *Alvin* provides an assessment of the quality of the underway measurements and of the data reduction procedures. The difference between bottom measurements and the nearest measurement on the underway traverses varied from 0.03 to 0.95 mGal with a mean of 0.37 ± 0.32 mGal (Figure 12a). The discrepancy in 11 of the 17 comparisons was <0.3 mGal and only four comparisons showed a difference of >0.5 mGal. Some of the mismatch may be due to across-track variations in the gravity field since we attempted to run straight traverses and therefore did not make sharp course changes in order to pass exactly over the markers. The distance between fixed markers and the closest point on the traverses varied from 0 to 93 m with a mean difference of 47 m. The mean gravity difference between the free-water anomaly at markers and on the traverses is 0.32 ± 0.29 mGal if only measurements within 60 m of a marker are considered (Figure 12b), and is 0.30 ± 0.30 mGal for measurements separated by <40 m. Thus

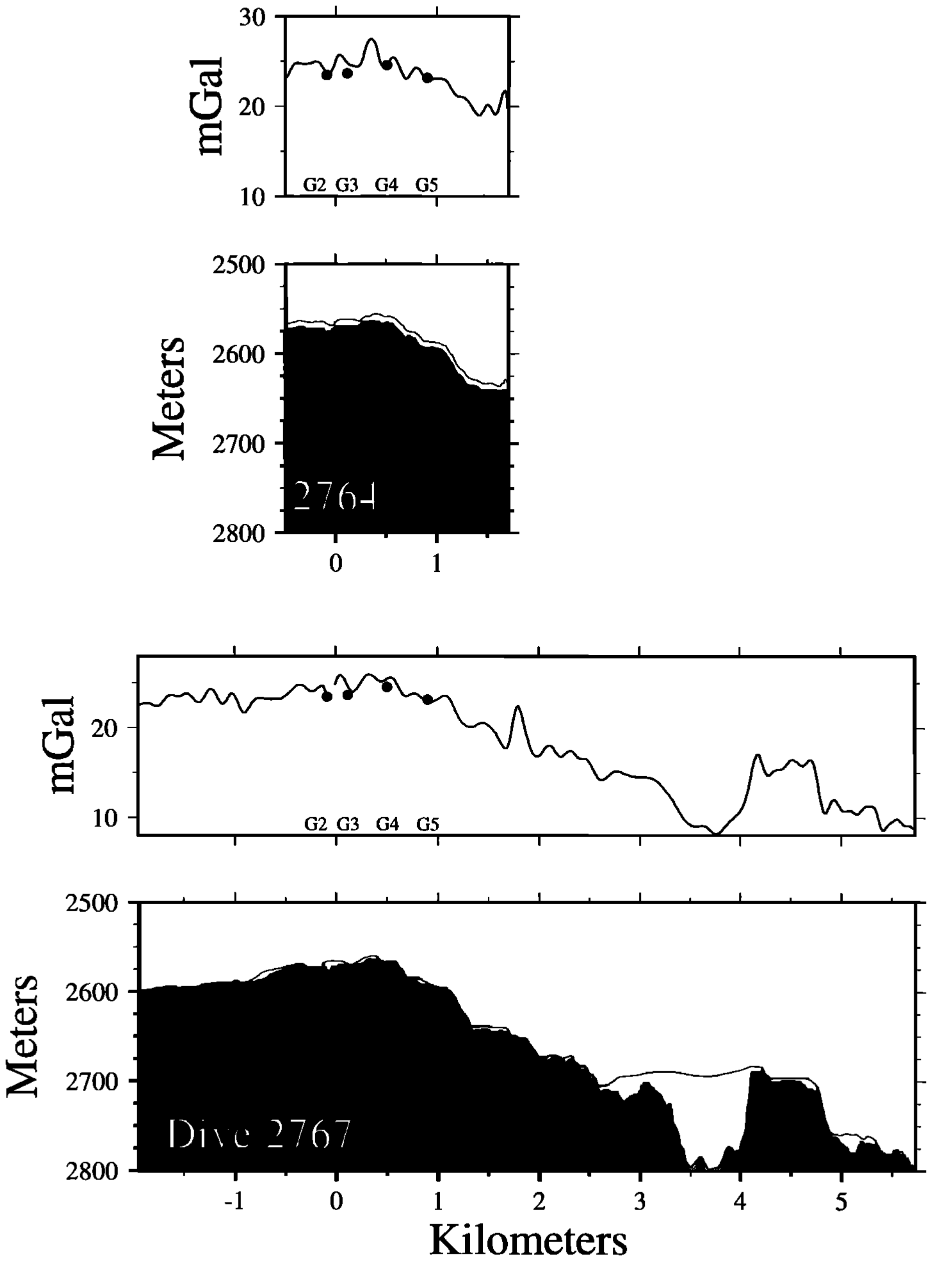

Figure 11a. Free-water gravity anomalies from near-bottom *Alvin* traverses in the 9°31'N area. Dive tracks are shown in Figure 3. Data have been projected along 82.4°, parallel to the local spreading direction. The origin for the projected profiles is the ASCT. The bottom diagram in each profile shows the observed bathymetry and the submersible's track over the seafloor. Light gray bathymetry near kilometer 3.5 on Dive 2767 is estimated from SeaBeam data where *Alvin* lost contact with the bottom. The top diagram for each profile shows free-water anomalies. The solid dots show the location and values of the free-water anomalies recorded at fixed bottom gravity stations.

some, but certainly not all of the difference in gravity values may be attributed to small-scale lateral variations in gravity in the upper crust in these areas. From this analysis, repeatability of measurements taken at the same location is of the order of 0.3 mGal.

The free-water anomalies show variations on two very different scales. There is a long-wavelength component which arises from changes in depth so that overall shape of free-water gravity profiles resembles the corresponding bathymetry profiles (Figures 11a and 11b). The bathymetry-related variation in free-water anomalies is of the order of 15 mGal in response to the 250- to 300-m depth variation in profiles 2767 and 2771 (Figures 11a and 11b). There are also much shorter wavelength anomalies, ~200-500 m across, with amplitudes of ~0.5 - 4 mGal on all four profiles which are not obviously related to the bathymetry. We interpret the shorter wavelength anomalies as arising from density variations within the upper crust.

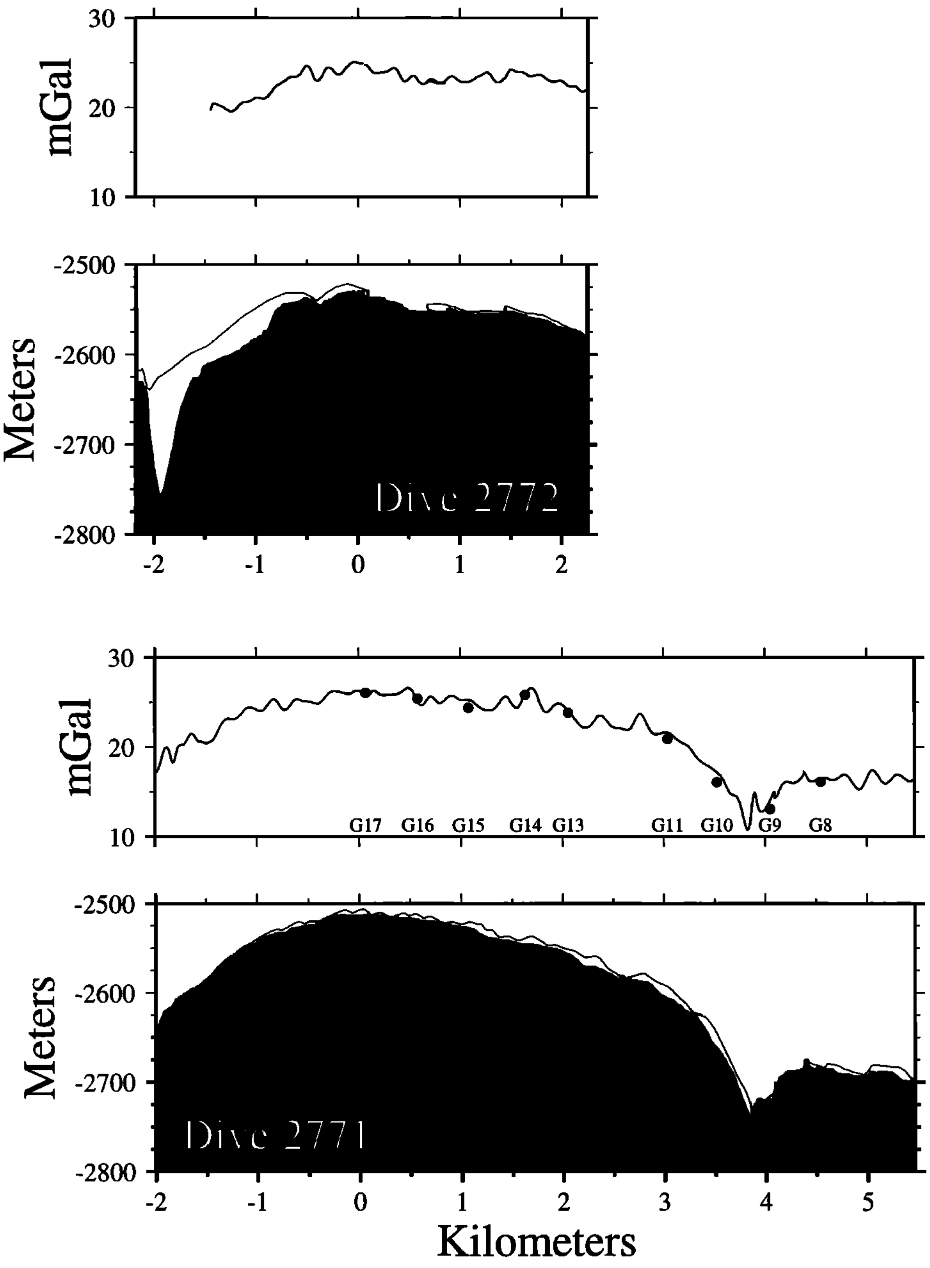

Figure 11b. Free-water gravity anomalies from near-bottom *Alvin* traverses in the 9°50'N area. Dive tracks are shown in Figure 4. Data have been projected along 82.4°, parallel to the local spreading direction. The origin for the projected profiles is the ASCT. The bottom diagram in each profile shows the observed bathymetry and the submersible's track over the seafloor. Light gray bathymetry near kilometer -2.0 on Dive 2772 is estimated from SeaBeam data where *Alvin* lost contact with the bottom. The top diagram for each profile shows free-water anomalies. The solid dots on the gravity profile for Dive 2771 show the location and values of the free-water anomalies recorded at fixed bottom gravity stations.

7. Bouguer Anomalies

The free-water correction accounts for the expected change in gravity with elevation resulting from the change in distance from the center of the Earth. It does not, however, account for the gravity effect of the corresponding change in the amount of mass between the observation point and a base level. As a result, the free-water anomalies show a correspondence to the topography (Figures 11a and 11b). An estimate of the density of the upper crustal rocks making up the topographic relief can be obtained from the relationship between free-air (or, in our case, free-water) anomalies and topography [*Nettleton*, 1939]. If the free-water anomalies arise primarily from topographic relief, then a plot of free-water anomaly against elevation will form a straight line with a slope given by $2\pi G(\rho_c - \rho_\omega)$, where ρ_c is the crustal density, ρ_ω is the density of seawater, and G is the gravitational constant.

Plots of free-water anomaly against depth are shown in Figure 13. Data from the southern dives near 9°31'N (Dives 2764 and 2767) are shown in gray and data from three of the northern dives at 9°50'N-9°52'N (Dives 2768, 2771, and 2772) are shown in black. Data from Dive 2770 were not included be-

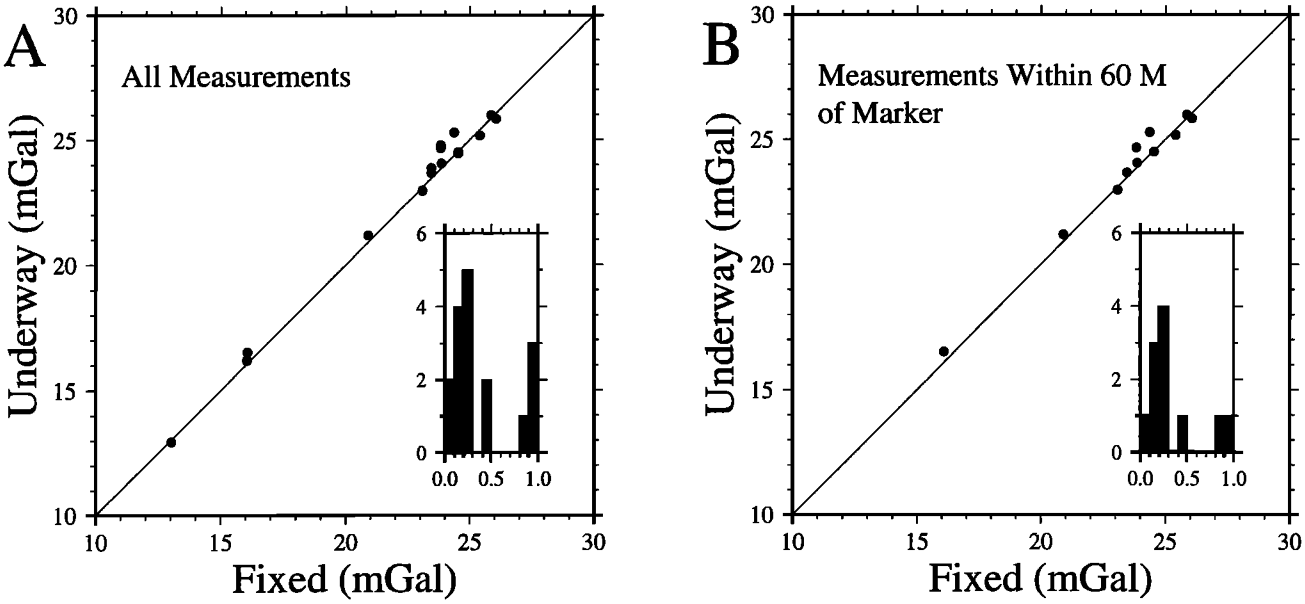

Figure 12. Comparison of free-water gravity anomalies measured while sitting on the bottom at fixed markers with underway free-water anomalies determined at the nearest point to the marker on *Alvin* traverses over the seafloor. The thin solid line illustrates an exact correspondence between fixed and underway measurements. The inset shows a histogram of the absolute value of the discrepancies. The left hand plot compares all measurements. Mean difference between fixed and underway measurements was 0.368 ± 0.323 mGal. The distance between the marker and the underway traverse varied from 0 to 93 m. The right hand plot shows the same comparison when only underway measurements within 60 m of the fixed sites are considered. The mean difference in this case is 0.324 ± 0.285 mGal. These data provide the basis for our considering the resolution of the continuous gravity data collected using the Bell gravimeter in Alvin to be ~0.3 mGal.

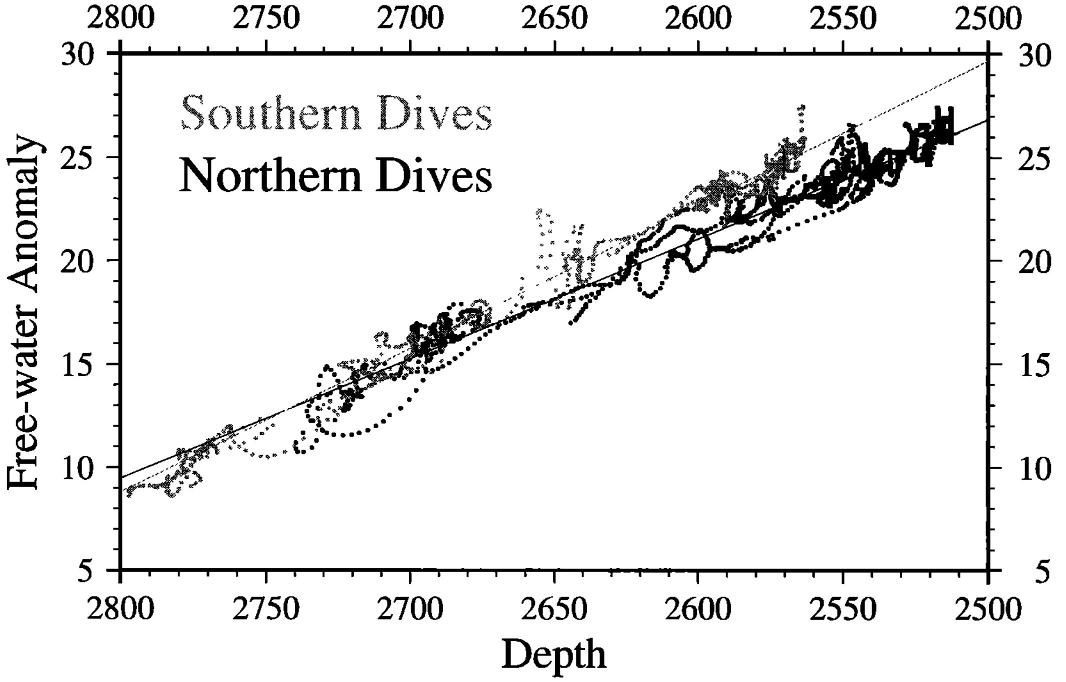

Figure 13. Plot of free-water gravity anomaly versus seafloor depth. Data from the northern dive sites (9°50'N-9°52'N) is in black, while data from the southern dive sites (9°31'N) is in gray. The solid line through each data set shows the best fitting linear relationship between gravity and depth. The slopes of these lines imply an upper crustal density of 2410 kg/m^3 for the 9°50'N area and 2669 kg/m^3 for the 9°31'N area.

cause there is less than 15 m of topographic relief along the entire dive track (Figure 3). The data from each area can be fit by straight lines, but the slopes of the lines from the two areas are different. An upper crustal density of 2690 kg/m^3 was obtained from data collected in the southern (9°31'N) area, while a value of 2410 kg/m^3 was calculated using data from the northern dive area near 9°50'N. Straight lines corresponding to both of these densities are shown superimposed on the data from both regions in Figure 13 to demonstrate the difference in the depth-gravity relationship between 9°31'N and 9°50'N.

Bathymetry and Bouguer anomaly profiles for the four across-axis traverses (Figures 3 and 4) are shown in Figures 14a and 14b. The Bouguer correction was calculated using a density contrast (ρ_c-ρ_ω) of 1660 kg/m^3 for Dives 2764 and 2767 and 1380 kg/m^3 for Dives 2771 and 2772. The long wavelength component of the free-water anomalies is completely removed by the Bouguer correction, which eliminates any obvious correlation between the observed gravity and morphology. The Bouguer anomalies have amplitudes of <4 mGal (generally, <2 mGal) and widths of a few hundred meters. The lack of Bouguer gravity anomalies at longer wavelengths implies that the crustal structure of the ridge crest is fairly homogenous laterally at scales of a few hundred meters to a few kilometers.

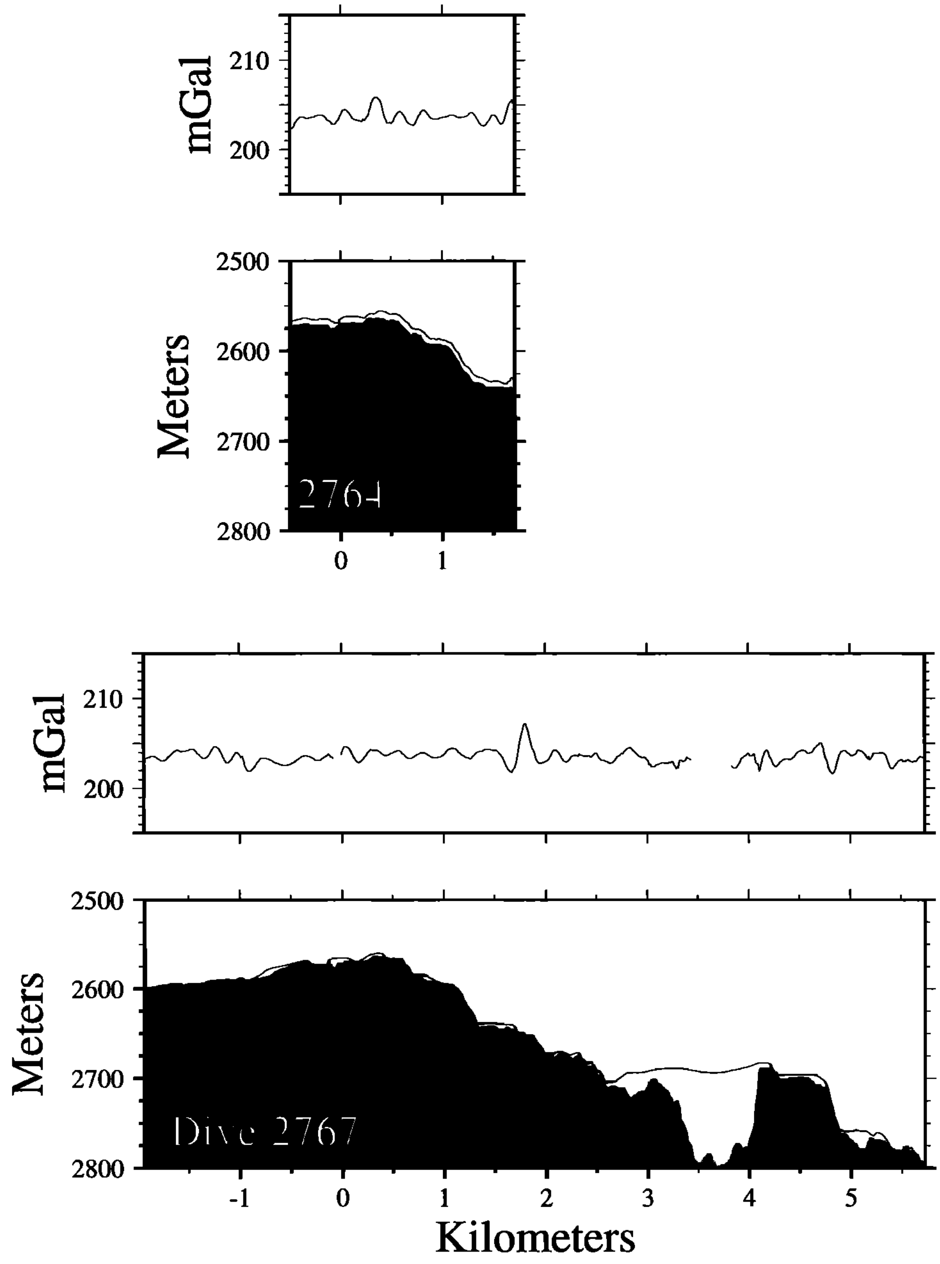

Figure 14a. Bouguer gravity anomalies from near-bottom *Alvin* traverses from the 9°31'N area. Dive tracks are shown in Figure 3. Data has been projected along 82.4°, parallel to the local spreading direction. The origin for the projected profiles is the ASCT. The bottom diagram in each profile shows the observed bathymetry and the submersible's track over the seafloor. Light gray bathymetry near kilometer 3.5 on Dive 2767 is estimated from SeaBeam data where *Alvin* lost contact with the bottom. The top diagram for each profile shows Bouguer anomalies. A density contrast of 1666 kg/m^3 between rock and seawater was used to calculate the Bouguer correction.

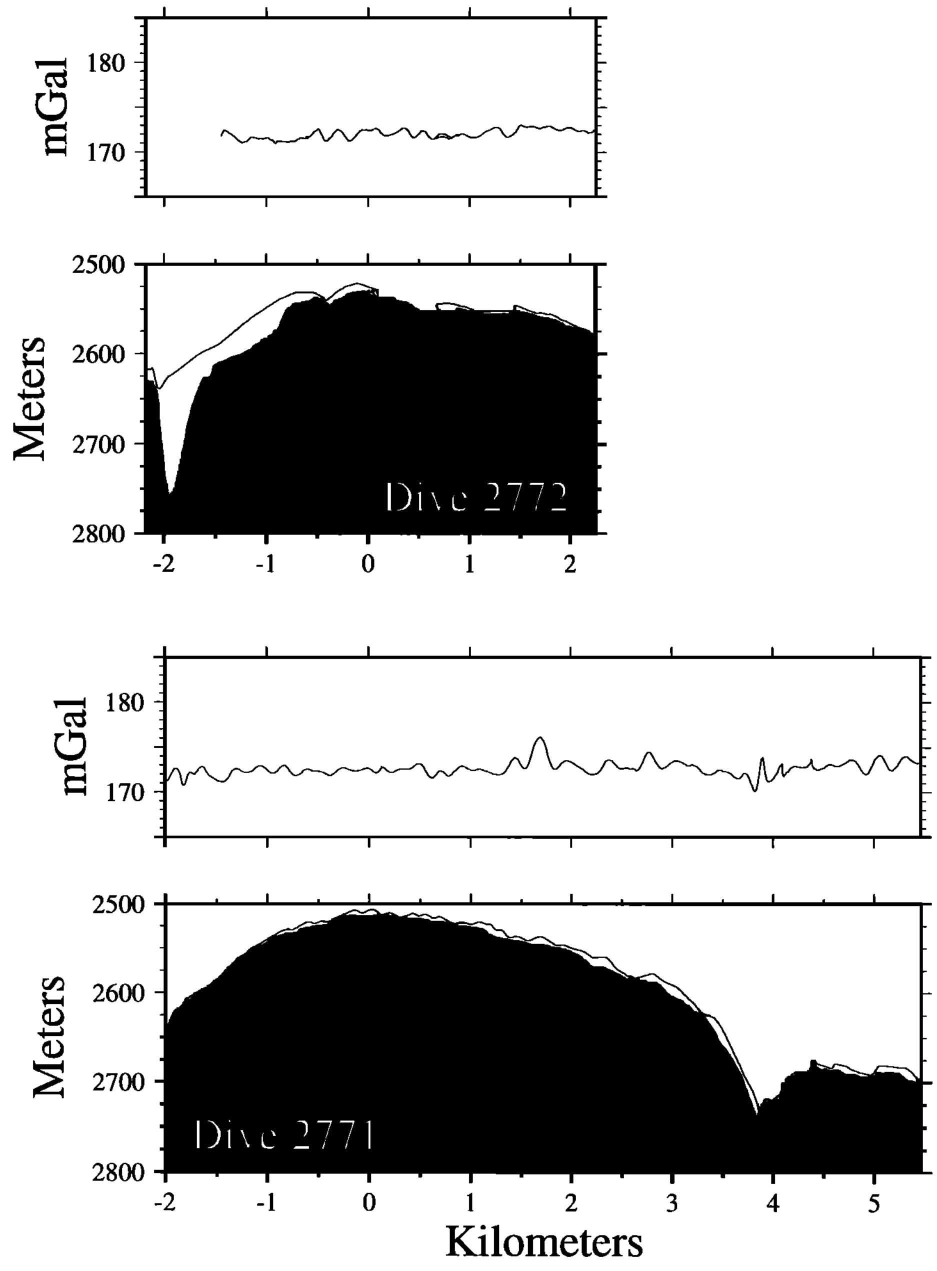

Figure 14b. Bouguer gravity anomalies from near-bottom *Alvin* traverses from the 9°50'N area. Dive tracks are shown in Figure 4. Data has been projected along 82.4°, parallel to the local spreading direction. The origin for the projected profiles is the ASCT. The bottom diagram in each profile shows the observed bathymetry and the submersible's track over the seafloor. Light gray bathymetry near kilometer -2.0 on Dive 2772 is estimated from SeaBeam data where *Alvin* lost contact with the bottom. The top diagram for each profile shows Bouguer anomalies. A density contrast of 1380 kg/m^3 between rock and seawater was used to calculate the Bouguer correction.

8. Discussion

8.1. Upper Crustal Density:

We obtained an upper crustal density of 2410 kg/m^3 for the EPR crest near 9°50'N and 2690 kg/m^3 for the southern area near 9°31'N. Nearly identical results were obtained whether the data for a region were combined or each dive was treated separately. There have been several previous estimates of upper crustal density at ridge axes from bottom gravity measurements using the *Nettleton* [1939] "density profiling" technique. These studies have generally deduced densities in the range of 2590 - 2660 kg/m^3 [*Luyendyk*, 1984; *Holmes and Johnson*, 1993; *Stevenson et al.*, 1994], slightly lower than, but consistent with, our determination of 2690 kg/m^3 for our southern dives. Our value of 2410 kg/m^3 for the 9°50'N area is considerably lower than most previous estimates. However, *Stevenson and Hildebrand* [1996] obtained a density of 2420 kg/m^3 from a set of 10 bottom gravity measurements extending from the axis to 20 km on the eastern flank at 9°48'N, just south of our dive area at 9°50'N.

A regional gravity gradient can affect the density determined using the *Nettleton* [1939] technique. A regional across-axis gravity gradient will decrease the estimated density obtained from data on one flank of the ridge and increase the density estimated with data from the other flank. If gravity and depth data from each ridge flank of the profile obtained on Dive 2771 (Figure 11b) are fit separately, an upper crustal density of 2420 kg/m^3 is obtained for data from the east flank and 2540 kg/m^3 is obtained for data from the west flank. The east flank data dominate the fit to the entire data set, since they extend over a much greater range of depths. The difference in density determined from each flank suggests that there might be a small regional across-axis gravity gradient at 9°50'N. If that is the case, then the actual density which would be determined in the absence of a regional gradient lies between those two estimates. This density is still significantly less than the estimate of 2690 kg/m^3 obtained at 9°31'N, or upper crustal density estimates obtained elsewhere at mid-ocean ridge crests. If the difference in density determined at 9°31'N and 9°50'N is due to an across-axis gravity gradient at 9°50'N, then the gradient would need to be 0.75 mGal/km. Surface ship gravity data [*Wang et al.*, 1996] suggest that if there is a regional across-axis gradient at 9°50'N, it is <0.1 mGal/km.

Upper crustal densities obtained from gravity studies in both regions are significantly less than whole-rock densities obtained directly from oceanic basalt samples, which are generally in the vicinity of 2900-3000 kg/m^3 [*Salisbury and Christensen*, 1978; *Warren and Rosendahl*, 1980; *Luyendyk*, 1984; *Holmes and Johnson*, 1993; *Johnson et al.*, 1996]. If the difference between whole-rock densities and those determined from the gravity anomalies is assumed to arise from porosity of the upper crust, then our results require that the bulk upper crustal porosity at 9°31'N is 11% and is 22% at 9°50'N, assuming a whole-rock density of 2900 kg/m^3. Other previous estimates of the porosity of upper crustal rocks from gravity studies are in the range of 10-23% [*Luyendyk*, 1984; *Holmes and Johnson*, 1993; *Stevenson et al.*, 1994; *Stevenson and Hildebrand*, 1996; *Johnson et al.*, 1996].

8.2. Upper Crustal Density and Layer 2A

Although the density determined from the *Nettleton* [1939] density profiling technique is the effective upper crustal density from a Bouguer gravity viewpoint, it is not necessarily the actual density of Layer 2A. Any distortion of the gravity field on the same spatial scale as the bathymetry will influence the estimate of density. *Stevenson and Hildebrand* [1996] pointed out that a buried density interface which follows seafloor relief will increase the apparent density determined from the free-water gravity versus depth relationship. In particular, the Layer 2A-2B boundary is a density interface that roughly parallels the seafloor at a depth shallow enough to have a significant gravity effect. Since Layer 2A thickens away from the axis [*Christeson et al.*, 1992; *Harding et al.*, 1993], the effect of the Layer 2A-2B boundary on the free-water versus depth gradient will be magnified because higher-density Layer 2B is closer to the seafloor at the axis where the largest free-water anomalies are found.

The Layer 2A-2B boundary has been mapped at both 9°31'N and 9°50'N from multichannel seismic reflection data [*Harding et al.*, 1993; *Vera and Diebold*, 1994]. Digitized Layer 2A thicknesses were added to the seafloor depths to give the depth to the Layer 2A-2B boundary, and the gravity effect of the interface was calculated at the location of the *Alvin* gravity measurements. We subtracted these values from the observed free-water anomalies and determined the slope of the residual free-water anomalies versus depth relationship. If a density contrast of 500 kg/m^3 is assumed across the Layer 2A-2B boundary, then the density deduced for Layer 2A from the residual free-water anomalies is reduced to 1980 kg/m^3 at 9°31'N and to 1730 kg/m^3 at 9°50'N. Smaller density contrasts across the Layer 2A-2B boundary produce correspondingly smaller density reductions and perhaps more realistic Layer 2A densities. However, the difference between the apparent upper crustal density at 9°50'N and 9°31'N remains at about 250 kg/m^3 and therefore is not the result of differing Layer 2A thickness or geometry at the two locations.

Since the 9°50'N area is the shallowest portion of the ridge axis in the segment and is volcanically and hydrothermally active, it could be argued that the lower slope of the gravity versus depth relationship at 9°50'N is the result of a difference in the thermal structure or magmatic/hydrothermal regime in the two regions. Higher temperatures and/or a higher melt fraction might be expected beneath the axis at 9°50'N than at 9°31'N. A decrease in the density of a trapezoidal region extending from the melt lens to the base of the crust, corresponding to the mush and transition zones of *Sinton and Detrick* [1992], can account for the difference in the free-water anomalies at 9°50'N and 9°31'N. However, if the low-density area is assumed to have an upper width of 1 km and a lower width of 10 km, consistent with thermal models [*Henstock et al.*, 1993; *Phipps Morgan and Chen*, 1993; *Magde et al.*, 1995], then the density difference needs to be 60 kg/m^3, which implies a temperature difference of over 700°K in the lower crust between 9°50'N and 9°31'N. If the density contrast is assumed to result from a larger melt fraction in the trapezoidal region, then the melt fraction needs to be 6-12% greater at 9°50'N than at 9°31'N, assuming a 100 -200 kg/m^3 density difference between melt and the crustal rocks. Both the inferred temperature difference and the increase in melt fraction appear too large to be reasonable, as are possible combinations of the two effects. The liquid magma lens has such a small gravity signal at the seafloor (< 0.1 mGal for a magma lens 1 km wide and 50 m thick at a distance of 1.5 km below the seafloor) that reasonable changes in its width or thickness would have virtually no effect on the gravity signal.

Christeson et al. [1992, 1994, 1996] used high-resolution on-bottom seismic refraction experiments to study the shallow crustal structure in the immediate vicinity of the EPR axis at 9°30'N. They found Layer 2A to consist of a "surficial low-velocity layer" with seismic velocity $V_p < 2.5$ km/s, separated by a high-gradient region from a layer with $V_p = 4.25 - 4.35$ km/s, which, in turn, is separated by another high-gradient region from Layer 2B with V_p of ~5.0 km/s. On the basis of submersible observations at Hess Deep [*Francheteau et al.*, 1992], *Christeson et al.* [1994] interpret the surficial layer as flows and pillow lavas and the 4.3 km/s layer as a combination of extrusives, dikes, and sills

The low-velocity surficial layer is very thin (<100 m), much less than the topographic relief (~300 m) along the cross-axis profiles, and has a nearly constant thickness away from the vicinity of the axis [*Christeson et al.*, 1992, 1994]. Thus the density determined from the relationship between the free-water anomalies and depth should probably be assigned to the 4.3-km/s layer rather than the surficial layer. The calculated density will still be affected by the deeper Layer 2A-2B boundary in the same manner as discussed above. However, the density contrast between the 4.3-km/s material and Layer 2B is considerably less, perhaps 200 kg/m^3. As a result, the effect of 2A-2B interface will have less influence on the gravity-elevation relationship. If a density contrast of 200 kg/m^3 is assumed for this interface, then the calculation described above yields 2410 kg/m^3 at 9°31'N and 2150 kg/m^3 at 9°50'N for the upper crustal density. Various empirical density-seismic velocity relationships derived from laboratory data [*Christensen and Shaw*, 1970; *Carlson and Raskin*, 1984; *Carlson and Herrick*, 1990] predict densities of 2400-2560 kg/m^3 for the V_P of 4.3 km/s determined by *Christeson et al.* [1994, 1996] at 9°30'N.

The difference in the relationship between free-water anomalies and depth at 9°31'N and 9°50'N does therefore appear to be significant and related to differences in the structure of the upper crust. There are a number of possible origins for this difference, including a significant variation in the porosity of the shallow crustal rock volume at different areas along the ridge crest, changes in the thickness of the low-velocity (and low-density) upper part of Layer 2A, and a difference in the proportion of low-density extrusives and higher-density dikes and sills within the main portion of Layer 2A. However, in the absence of detailed seismic studies at 9°50'N, such as have been undertaken at 9°30'N [*Toomey et al.*, 1990; *Christeson et al.*, 1992, 1994, 1996], it is not possible to verify or distinguish between different hypotheses.

8.3. Bouguer Gravity Anomalies and the Structure of the Uppermost Crust

The main feature of the Bouguer anomaly profiles across the EPR axis is a series of small gravity anomalies a few hundred meters across with amplitudes of 0.5 - 2 mGal (Figures 14a and 14b). Density variations within the uppermost crust could arise from areas of collapsed and fissured terrain separated by somewhat higher density flows, or zones of intrusion and subsurface diking which fed volcanic eruptions at or near the axis. Fissuring and collapse are observed [*Fornari et al.*, 1998] and gravity modeling (Figures 15a-15c) shows that lateral density contrasts arising in this manner may result in observable gravity anomalies. However, for realistic density contrasts and geometries the gravity anomalies are less than about 0.9 mGal. This suggests that although density variations due to fissuring and collapse could contribute to the observed gravity anomalies, they are unlikely to be the sole cause.

Large positive gravity anomalies with amplitudes of about 4 mGal were found at two locations, ~1.85 km east of the axis on Dive 2767 (near 9°31'N) and ~1.75 km east of the axis on Dive 2771 (near 9°50'N) (Figures 14a and 14b). Both locations are characterized by linear ridges (~10 m high and ~50 m wide) of fresh, glassy pillow lavas [*Perfit et al.*, 1994; *Fornari and Embley*, 1995; *Fornari et al.*, 1998] which, on the basis of observational data, appear to be recent off-axis volcanic constructions. Since the observed morphologic expression of

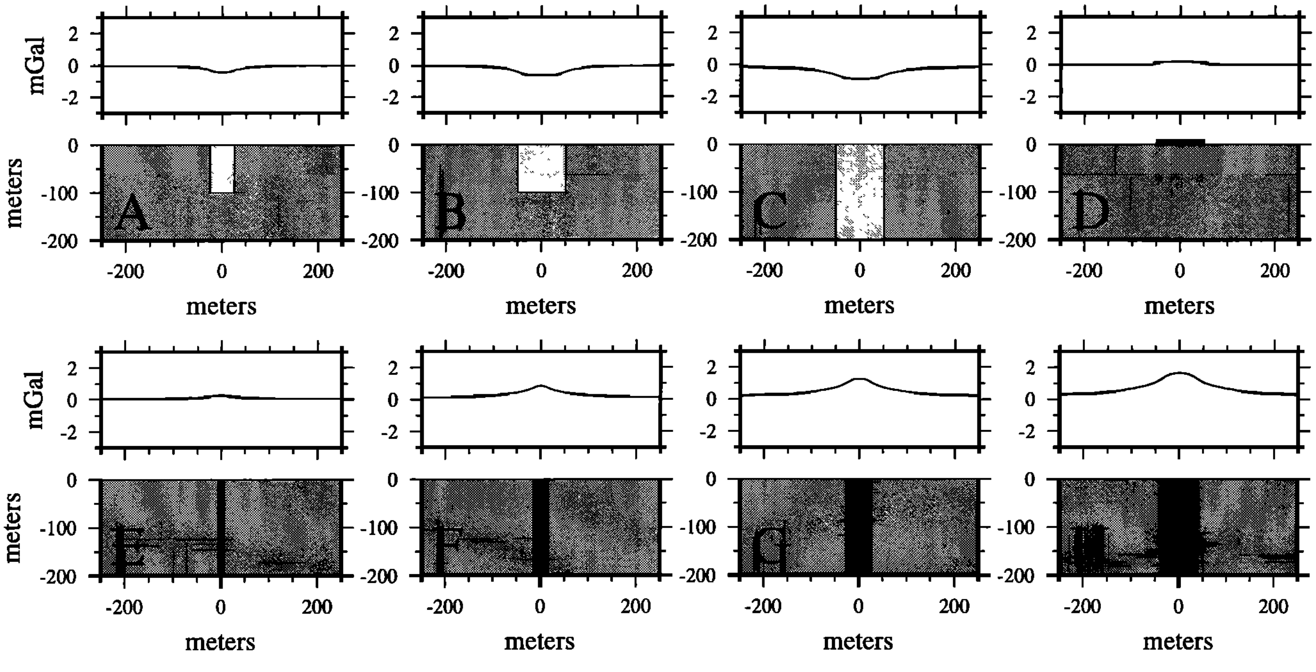

Figure 15. Model gravity anomalies arising from hypothetical two-dimensional geologic structures. All anomalies are calculated at a distance of 5 m above the seafloor. Models A-C represent regions of fissuring or low-density flows with a density contrast of -300 kg/m^3 with the surrounding area. In Model A the low-density area is 50 m wide and extends to a depth of 100 m, in Model B it is 100 m wide and extends to a depth of 100 m, and in Model C it is 100 m wide and extends to 200 m. These three models produce gravity anomalies of -0.43, -0.65, and -0.91 mGal. Model D is a high-density flow (density contrast of 600 kg/m^3) 10 m thick and 100 m wide. It produces an anomaly of 0.22 mGal, which probably could not be resolved. Models E-H represent dike swarms with a density contrast of 600 kg/m^3 extending to a depth of 300 m. The width of the dike swarm is assumed to be (E) 10 m, (F) 30 m, (G) 50 m, and (H) 70 m. They produce anomalies of 0.32, 0.85, 1.28, and 1.65 mGal, respectively.

these suspected off-axis eruptions is small and is accounted for in the Bouguer correction, we interpret the Bouguer gravity anomaly at these sites as arising primarily from dike swarms feeding the off-axis volcanism. The modeling shown in Figure 15d suggests that if these volcanic constructs were simply surficial mounds of slightly higher density pillows, their near-bottom Bouguer gravity signature would be small (~0.2 mGal) and unlike the observed anomalies. The observation of large-amplitude gravity anomalies at these sites provides support for the hypothesis that these features are created by off-axis eruptions sourced by dikes beneath the pillow ridges and are not parasitic vents fed via subsurface tubes or channels from the ASCT.

Figures 16a and 16b show the free-water and Bouguer gravity anomalies mapped during the grid survey of the axis at 9°50'N (Figure 4). These anomalies can be correlated between tracks and appear to be lineated parallel to the axis for at least a distance of nearly a kilometer. Axis-parallel lineated anomalies suggest dikes feeding lava to the axis as a possible source of the gravity anomalies. Axis-parallel bands of low density, fissured crust may also be present, but for reasonable density contrasts and geometry they cannot by themselves result in the observed amplitude of gravity anomalies. If the anomalies are assumed to arise from dikes, then the dikes must form swarms since a single dike has a negligible gravity effect. The observed gravity anomalies in the ASCT grid survey (Figures 16a and 16b) can be reproduced by dike swarms with widths of 40-100 m and a density contrast of ~600 kg/m^3 (i.e., 2900 kg/m^3 for dikes, 2300 kg/m^3 for flows) (Figure 15).

Although the anomalies recorded during the ASCT survey are lineated along the axis, the amplitude of the anomalies varies from about 0.5 to 1.6 mGal within a distance of a few hundred meters. The along-strike changes in anomaly amplitude may be related to variations in the depth to the top of a dike swarm. In this case, we expect that along-axis gravity highs will be associated with regions of recent volcanic eruption. This possibility is suggested by the observation that the gravity high we mapped just east of the ASCT near 9°50.3'N (Figures 16a and16b) overlies a subtle topographic high which has been attributed to volcanic construction during the 1991 eruption [*Fornari and Embley*, 1995; *Fornari et al.*, 1998].

The coincidence of the gravity high at 9°50.3'N with extrusive volcanism supports the interpretation that small axis-parallel gravity anomalies result from zones of concentrated dike injection. At the EPR at 9°30'-9°50'N, a 50-m-wide dike swarm represents ~455 years of extension. Consequently, if the anomalies do arise from dike swarms, one implication would be that the eruptive axis remains spatially stable for 350-900 years and then jumps, perhaps by 100 m or so, leaving an area made up primarily of flows and variably collapsed terrain between the intrusive zones. When buried by later flows, this lateral mixture of dike swarms and flows could make up the lower 4.3 km/s portion of Layer 2A [*Christeson et al.*, 1994].

Figures 16a and 16b also show the location of the ASCT walls as picked by *Fornari et al.* [1990, 1998] on the basis of Argo I and *Alvin* observations. The ASCT has a small 75-m lateral offset near 9°50.15'N (Figures 16a and 16b), and also changes character at this offset, becoming shallower and less well developed to the south [*Fornari et al.*, 1998, see their Figure 2]. The offset is also associated with a disruption of the along-axis pattern of Bouguer gravity anomalies (Figure 16b). Anomalies on across-axis gravity profiles can be correlated from line-to-line on either side of the offset, but the pattern changes significantly at the offset (Figure 16b).

Fornari et al. [1998] developed a four-stage model for the evolution of different axial summit trough morphologies observed on the fast spreading EPR crest, emphasizing the role of volcanic collapse of the crustal carapace. *Chadwick* [1997] and *Chadwick and Embley* [1998] have emphasized the role of faulting immediately above an intruding dike in the formation of axial summit depressions. In both models, there is a direct relationship between dike injection, lava emplacement, and the ASCT. Eruptive fissures are often observed within or immediately adjacent to the ASCT [*Haymon et al.*, 1993; *Fornari and Embley*, 1995; *Chadwick and Embley*, 1998; *Fornari et al.*, 1998], supporting a direct relationship.

It is thus possible that the offset and change in character of the ASCT and the disruption of the along-axis pattern of Bouguer gravity anomalies (Figure 16b) are related and, in fact, are both reflections of segmentation of the shallow feeders which deliver magma to the seafloor. It is believed that much of the ridge axis from ~9°45'N to 9°51'N erupted in 1991/1992 [*Haymon et al.*, 1993; *Rubin et al.*, 1994; *Gregg et al.*, 1996]. The deeper portion of the magma supply system (magma chamber and sheeted dikes) is probably continuous for that entire 8.5 km length of ridge axis, allowing efficient along-axis transport of melt. The observations in Figure 16b suggest that the shallower portion of the supply system (dikes up through Layer 2A to the surface) may be segmented on a finer scale.

9. Summary and Conclusions

High-resolution, continuous underway near-bottom gravity anomaly data, which can be used to investigate the density distribution in shallow oceanic crust, can be obtained from a research submersible. We utilized a Bell Aerospace BGM-3 gravimeter mounted within the personnel sphere of DSV *Alvin* to collect gravity data at an altitude of ~3-7 m above the seafloor along more than 35 km of track located on the crest and upper flanks of the EPR at 9°31'N and 9°50'N (Figures 3 and 4). Gravity measurements along profiles up to 8 km long may be obtained on one dive (Figures 3, 4, 11a and 11b). A comparison of gravity measurements obtained at fixed bottom markers and during underway traverses over the markers indicates that the repeatability of measurements made at the same location on different dives is about 0.3 mGal (Figure 12).

Along-track spatial resolution of anomalies is about 130-160 m. The limiting factor on spatial resolution in these data is low-pass filtering necessary to remove high-frequency noise resulting from limitations on the precision and sampling rate of the pressure gauge depth data used to calculate the vertical motions of the submersible. Model studies suggest that modifications subsequently implemented in the *Alvin* data logging system will eliminate the need for the low-pass filtering and allow detection of shorter-wavelength gravity anomalies in future studies which use this technique.

The average upper crustal density obtained from the slope of the relationship between free-water anomaly and depth on the EPR crest varies significantly between 9°31'N and 9°50'N. We calculated an average upper crustal density of 2410 kg/m^3 for the 9°50'N area and 2690 kg/m^3 for the 9°31'N area. Previous estimates of the upper crustal density based on bottom gravity measurements [*Luyendyk*, 1984; *Holmes and Johnson*, 1993; *Stevenson et al.*, 1994] have generally given densities in the

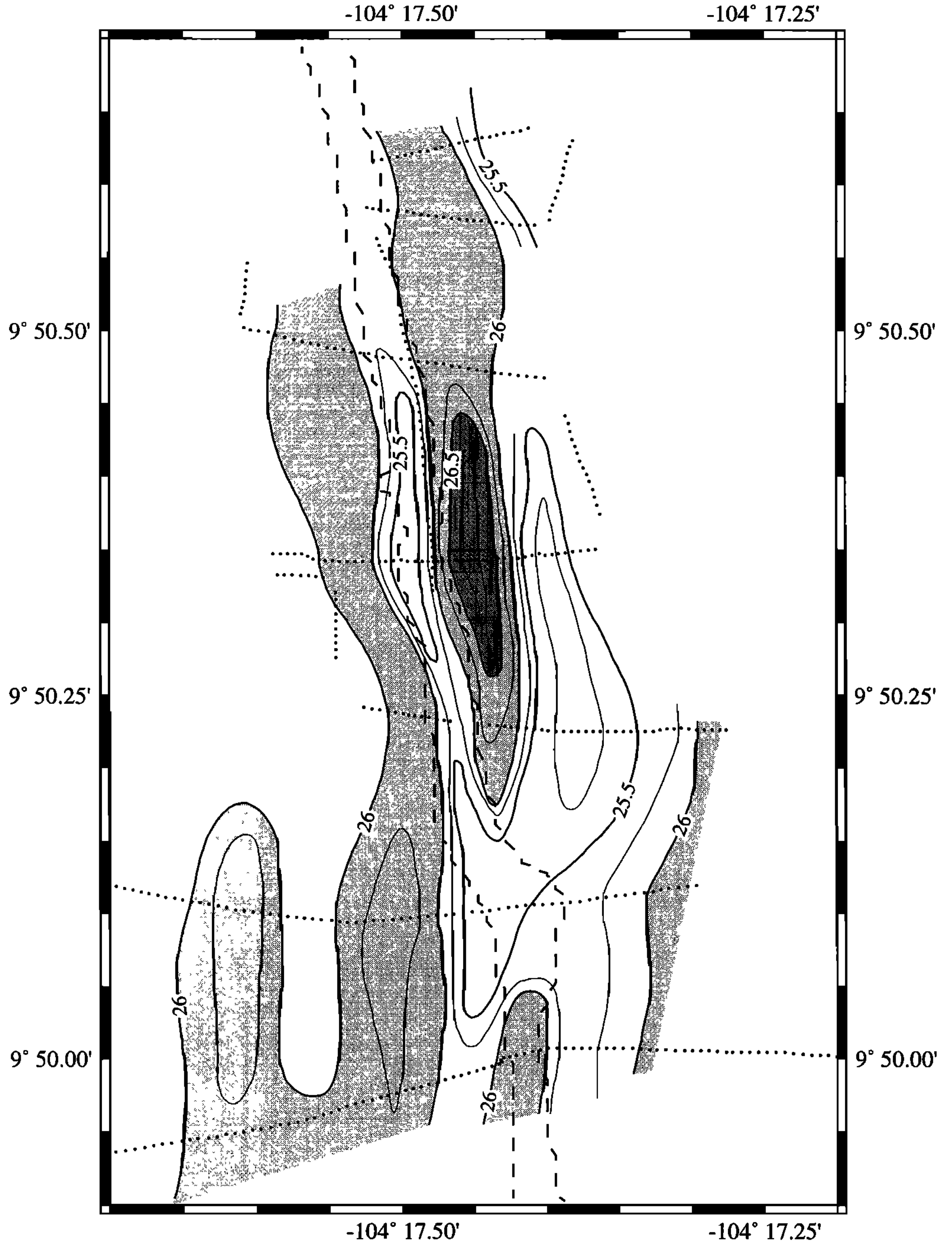

Figure 16a. Free-water gravity anomaly map of the crest of the EPR from 9°49.9'N to 9°50.7'N, contoured at 0.25-mGal intervals. Areas of gravity anomalies > 26.0 mGal are shaded light gray, and areas of gravity anomalies > 26.5 mGal are shaded dark gray. Dots show location of near-bottom gravity measurements used in construction of the map. Dashed lines show the location of the ASCT walls as picked by *Fornari et al.* [1990, 1998] on the basis of Argo-I and *Alvin* observations in 1989, 1991, and 1992. Note the ~75 m offset of the ASCT near 9°50.15'N.

range of 2600-2700 kg/m^3, consistent with our determination at 9°31'N. However, a density estimate at 9°48'N on the EPR axis by *Stevenson and Hildebrand* [1996] also produced a value of 2420 kg/m^3. The difference in estimated upper crustal density between the two regions is not the result of an across-axis gravity gradient affecting one of the areas. The difference between the average upper crustal density estimated for the 9°31'N and 9°50'N areas is also not the result of differing Layer 2A-2B boundary geometry and is unlikely to result from a difference in the thermal structure of the lower crust in the two regions. Possible explanations for the different effective upper crustal densities at 9°31'N and 9°50'N include a difference in the average upper crustal porosity, a difference in the thickness of the low-velocity (and low-density) upper "surficial"

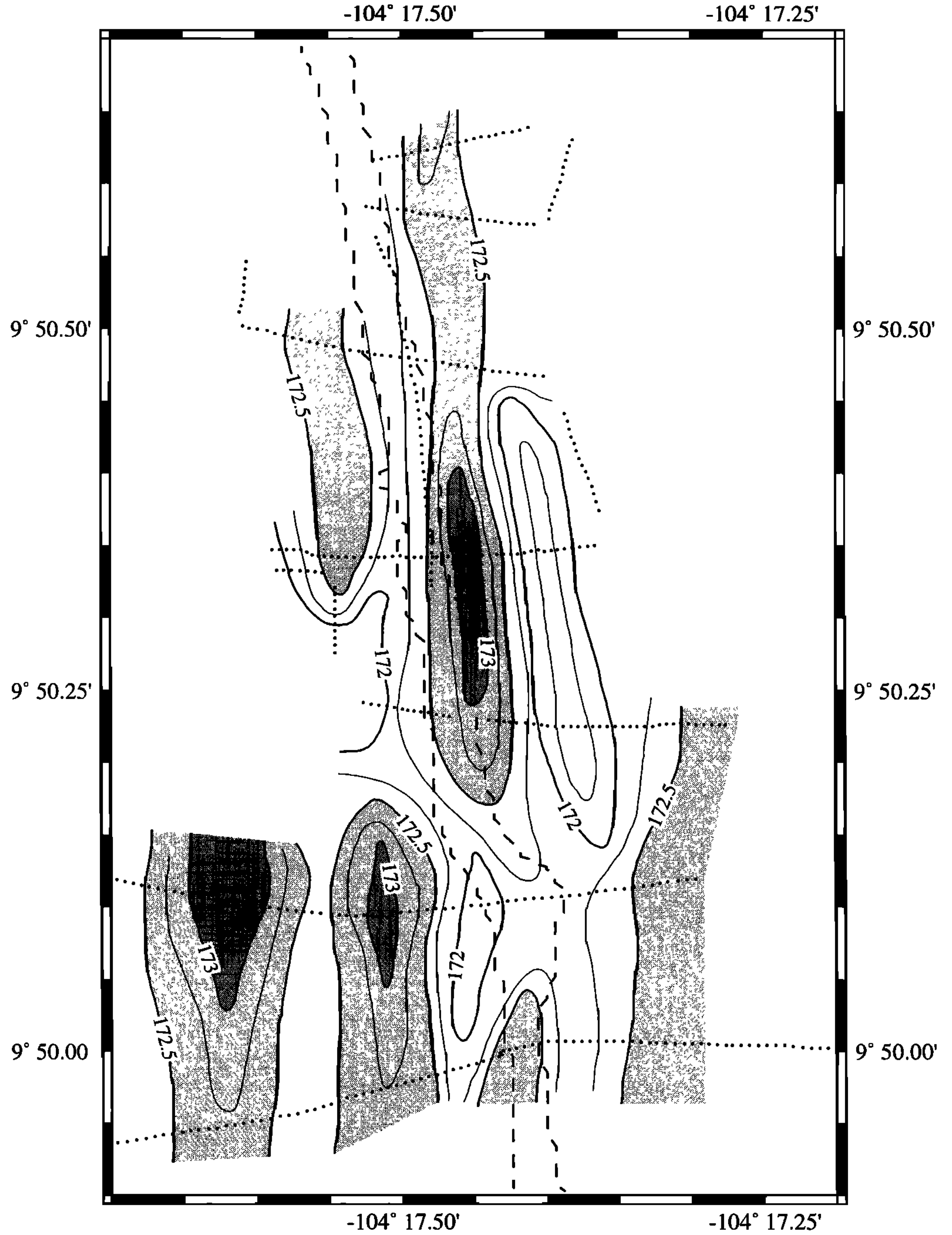

Figure 16b. Bouguer gravity anomaly map of the crest of the EPR from 9°49.9'N to 9°50.7'N, contoured at 0.25-mGal intervals. A crust-water density contrast of 1380 kg/m^3 was assumed in calculation of the Bouguer anomalies. Areas of gravity anomalies > 172.5 mGal are shaded light gray, and areas of gravity anomalies > 173.0 mGal are shaded dark gray. Dots show location of near-bottom gravity measurements used in construction of the map. Dashed lines show the location of the ASCT walls as picked by *Fornari et al.* [1990, 1998]] on the basis of Argo-I and *Alvin* observations in 1989, 1991, and 1992. Note ~75 m offset of the ASCT near 9°50.15'N.

part of Layer 2A, or a difference in the proportion of lower-density extrusives and higher-density dikes and sills with the main portion of Layer 2A.

The Bouguer gravity anomalies near the EPR axis at 9°31'N and 9°50'N are characterized by small anomalies a few hundred meters across with amplitudes of 0.5-2 mGal (Figures 14a and14b). Larger amplitude anomalies of ~4 mGal are found at a few locations situated 1-2 km off-axis. Sources which could contribute to the small-amplitude anomalies include low-density areas of collapsed and fissured terrain and high-density dike swarms which fed eruptions. The larger off-axis anomalies are associated with pillow ridges composed of lavas which are clearly younger than the surrounding seafloor and which have distinct chemical compositions compared to lavas from the ASCT at the same latitude [*Perfit et al.*, 1994]. These anomalies are interpreted to arise from dike swarms feeding off-axis eruptions.

A grid survey of the ridge axis between 9°49.95'N and 9°50.65'N shows that the Bouguer anomalies in that region are lineated parallel to the axis, suggesting that axis-parallel dike swarms contribute to the observed gravity anomalies. The pattern of gravity anomalies is disrupted and offset at a 75-m offset of the ASCT near 9°50.15'N (Figure 16b). The coincidence of an offset in both the gravity anomalies and the ASCT, both of which may be related to dikes feeding eruptions at the axis, suggests that the shallow portion of the magma supply system (dikes through Layer 2A to the surface) may be segmented on a finer scale than the deeper magmatic system.

Acknowledgments. We thank the officers and crew of the R/V *Atlantis-II*, the shipboard *Alvin* pilots and crew, and shore-based deep submergence operations group for *Alvin*, who were all instrumental in the technical support of the vehicles and helping us with the installation of the NAVOCEANO gravimeter. Their dedication and high level of expertise are, as always, greatly appreciated. Bob Grieve and Pat Hickey were especially helpful at sea, as were Dudley Foster and Lane Abrams on shore with the details of integrating and operating the BGM-3 gravimeter in *Alvin*. We gratefully acknowledge the field support and collaboration of the U.S. Naval Oceanographic Office in providing the Bell BGM-3 gravimeter used for this work, and R. Pittenger for assisting in coordinating its use. Tracy Gregg assisted in data compilation and field support during the *Alvin* dives. Support for the field programs and shore-based data analysis were provided by NSF grants OCE93148666 (J.R.C.) and OCE9408904 (D.J.F). LDEO contribution 5909. Woods Hole contribution 9890.

References

Barth, J. A., K. A Kastens, and E. M. Klein, The origin of bathymetric highs at ridge-transform intersections: A multi-disciplinary case study at the Clipperton fracture zone, *Mar. Geophys. Res.*, *16*, 1-50, 1994.

Bell, R. E., and A. B. Watts, Evaluation of the BGM-3 sea gravity meter system onboard R/V *Conrad*, *Geophysics*, *51*, 1480-1493, 1986.

Carbotte, S., and K. C. Macdonald, East Pacific Rise 8°N-10°30'N: Evolution of ridge segments and discontinuities from SeaMARC II and three-dimensional magnetic studies, *J. Geophys. Res.*, *97*, 6959-6982, 1992.

Carlson, R. L., and C. N. Herrick, Densities and porosities in the oceanic crust and their variations with depth and age, *J. Geophys. Res.*, *95*, 9153-9170, 1990.

Carlson, R. L., and G. S. Raskin, Density of the oceanic crust, *Nature*, *311*, 555-558, 1984.

Chadwick, W. W., Is the "axial summit caldera" on the East Pacific Rise really a "graben"?, *RIDGE Events*, *8*, 8-11, 1997.

Chadwick, W. W., and R. W. Embley, Graben formation associated with recent dike intrusions and volcanic eruptions on the mid-ocean ridge, *J. Geophys. Res.*, *103*, 9807-9825, 1998.

Christensen, N. I., and G. H. Shaw, Elasticity of mafic rocks from the mid-Atlantic ridge, *Geophys. J. R. astron. Soc.*, *20*, 271-284, 1970.

Christeson, G. L., G. M. Purdy, and G. J. Fryer, Structure of young upper crust at the East Pacific Rise near 9°30'N, *Geophys. Res. Lett.*, *19*, 1045-1048, 1992.

Christeson, G. L., G. M. Purdy, and G. J. Fryer, Seismic constraints on shallow crustal emplacement processes at the fast spreading East Pacific Rise, *J. Geophys. Res.*, *99*, 17,957-17,973, 1994.

Christeson, G L., G. M. Kent, G. M. Purdy, and R. S. Detrick, Extrusive thickness variability at the East Pacific Rise, 9° - 10°N: Constraints from seismic techniques, *J. Geophys. Res.*, *101*, 2859-2873, 1996.

Detrick, R. S., P. Buhl, E. E Vera, J. C. Mutter, J. A. Orcutt, J. A. Madsen, and T. M Brocher, Multichannel seismic imaging of the axial magma chamber along the East Pacific Rise between 9°N and 13°N, *Nature*, *326*, 35-41, 1987.

Evans, R. L., A seafloor gravity profile across the TAG hydrothermal mound, *Geophys. Res. Lett.*, *23*, 3447-3450, 1996.

Fornari, D. F., and R. W. Embley, Tectonic and volcanic controls on hydrothermal processes at the mid-ocean ridge:; An overview based on near-bottom and submersible studies, in *Seafloor Hydrothermal Systems: Physical, Chemical, Biological, and Geological Interactions*, Geophys. Monogr. Ser., vol 91, edited S.E. Humphries et al., pp. 1-46, AGU, Washington, D.C., 1995.

Fornari, D. J., R. M. Haymon, M. E. Edwards, and K. C. Macdonald, Volcanic and tectonic characteristics of the East Pacific Ride crest 9°09'N-9°54'N: Implications for the fine-scale segmentation of the plate boundary (abstract), *Eos Trans. AGU*, *71*, 625, 1990.

Fornari, D. J., R. M. Haymon, M. R. Perfit, T. K. P. Gregg, and M. H. Edwards, Axial summit trough of the East Pacific Rise 9°N-10°N: Geological characteristics and evolution of the axial zone on fast spreading mid-ocean ridges, *J. Geophys. Res.*, *103*, 9827-9855, 1998.

Francheteau, J., R. Armijo, J. L. Cheminée, P. Hekinian, P. Lonsdale, and N. Blum, Dyke complex of the East Pacific Rise exposed in the walls of Hess Deep and the structure of the upper oceanic crust, *Earth Planet. Sci. Lett.*, *111*, 109-121, 1992.

Gass, I. G., Magmatic processes at and near constructive plate margins as deduced from the Troodos (Cyprus) and Semail Nappe (N. Oman) ophiolites, in *Magmatism in the Ocean Basins*, edited by A. D. Saunders and M. J. Norry,*Geol. Soc. Spec. Publ.*, *42*, 1-15 1989.

Gregg, T. K. P., D. J. Fornari, M. R. Perfit, R. M. Haymon, and J. H. Fink, Rapid emplacement of a mid-ocean ridge lava flow on the East Pacific Rise at 9°46'-51'N, *Earth Planet. Sci. Lett.*, *144*, E1-E7, 1996.

Harding, A. J., G. M. Kent, and J. A. Orcutt, A multichannel seismic investigation of the upper crustal structure at 9°N on the East Pacific Rise: Implications for crustal accretion, *J. Geophys. Res.*, *98*, 13,925-13,944, 1993.

Haymon, R. M., The response of ridge crest hydrothermal systems to segmented, episodic magma supply, in *Tectonic, Magmatic and Biological Segmentation of Mid-ocean Ridges*, *Geol. Soc. Spec. Publ.*, *118*, edited by C. J. Macleod, P. A. Tyler and C. L. Walker, 157-168, 1996.

Haymon, R. M., D. J. Fornari, M. H. Edwards, S. Carbotte, D. Wright, and K. C. Macdonald, Hydrothermal vent distribution along the East Pacific Rise crest (9°09'-54'N) and its relationship to magmatic and tectonic processes on fast-spreading mid-ocean ridges, *Earth Planet. Sci. Lett.*, *104*, 513-534, 1991.

Haymon, R. M., et al., Volcanic eruption of the mid-ocean ridge along the East Pacific Rise at 9°45'-52'N: Direct submersible observation of seafloor phenomena associated with an eruption event in April, 1991, *Earth. Planet. Sci. Lett.*, *119*, 85-101, 1993.

Henstock, T. J., A. W. Woods, and R. S. White, The accretion of oceanic crust by episodic sill intrusion, *J. Geophys. Res.*, *98*, 4131-4161, 1993.

Hildebrand, J. A., J. M. Stevenson, P. T. C. Hammer, M. A. Zumberge, R. L. Parker, C. G. Fox, and P. J. Meis, A seafloor and sea surface gravity survey of Axial Volcano, *J. Geophys. Res.*, *95*, 12,751-12,763, 1990.

Holmes, M. L., and H. P. Johnson, Upper crustal densities derived from bottom gravity measurements: Northern Juan de Fuca Ridge, *Geophys. Res. Lett.*, *20*, 1871-1874, 1993.

Johnson, H. P., D. Van Patton, and M. T. Tivey, Structure of upper oceanic crust from seafloor gravity measurements near the Blanco transform (abstract), *Eos Trans. AGU*, *77*(46), Fall Meet. Suppl. F707, 1996.

Kidd, R. G. W., A model for the formation of the upper oceanic crust, *Geophys. J. R. Astron. Soc*, *50*, 159-153, 1977.

Langmuir, C. H., J. F. Bender, and R. Batiza, Petrological and tectonic segmentation of the East Pacific Rise, 5°30'-14°30'N, *Nature*, *322*, 422-429, 1986.

Luyendyk, B. P., On-bottom gravity profile across the East Pacific Rise crest at 21°North, *Geophysics*, *49*, 2166-2177, 1984.

Macdonald, K. C., and P. J. Fox, The axial summit graben and cross-sectional shape of the East Pacific Rise as indicators of axial magma chambers and recent volcanic eruptions, *Earth Planet. Sci. Lett.*, *88*, 119-131, 1988.

Macdonald, K. C., P. J. Fox, L. J. Perram, M. F. Eisen, R. M. Haymon, S. P. Miller, S. M. Carbotte, M. H. Cormier, and A. N. Shor, A new view of the mid-ocean ridge from the behaviour of ridge-axis discontinuities, *Nature*, *335*, 217-225, 1988.

Magde, L. S., R. S. Detrick, G. M. Kent, A. J. Harding, J. A. Orcutt, J. C. Mutter, and P. Buhl, Crustal and upper mantle contribution to the axial gravity anomaly at the southern East Pacific Rise, *J. Geophys. Res.*, *100*, 3747-3766, 1995.

Nettleton, L. L., Determination of density for reduction of gravimeter measurements, *Geophysics, 4,* 176-183, 1939.

Perfit, M. R., D. J. Fornari, M. C. Smith, J. F. Bender, C. H. Langmuir, and R. M. Haymon, Small-scale spatial and temporal variations in mid-ocean ridge crest magmatic processes, *Geology, 22,* 375-379, 1994.

Phipps Morgan, J., and Y. J. Chen, The genesis of oceanic crust: Magma injection, hydrothermal circulation, and crustal flow, *J. Geophys. Res., 98,* 6283-6297, 1993.

Rubin, K. H., J. D. Macdougall, and M. R. Perfit, ^{210}Po-^{210}Pb dating of recent volcanic eruptions on the sea floor, *Nature, 368,* 842-844, 1994.

Salisbury, M. H., and N. I. Christensen, The seismic velocity of a traverse through the Bay of Islands Ophiolite Complex, Newfoundland, an exposure of oceanic crust and upper mantle, *J. Geophys. Res*, *83,* 805-817, 1978.

Scheirer, D. S., and K. C. Macdonald, Variation in cross-sectional area of the axial ridge along the East Pacific Rise: Evidence for the magmatic budget of a fast spreading center, *J. Geophys. Res., 98,* 7871-7885, 1993.

Schouten, H., M. Tivey, D. Fornari, and J. R. Cochran, The Central Anomaly Magnetic High: Constraints on the volcanic construction of seismic Layer 2A at a fast-spreading mid-ocean ridge, *Earth Planet. Sci. Lett., in press,* 1999.

Shank, T. M., R. A. Lutz, D. J. Fornari, R. M. Haymon, M. Lilly, K. Von Damm, M. R. Perfit, M. H. Edwards, W. C. Shanks, and D. D., Rapid development of biological community structure and associated geochemical and geological features at hydrothermal vents at 9°N-10°N, East Pacific Rise (abstract), *Eos Trans. AGU), 75*(44), Fall Meet. Suppl., 601, 1994.

Shank, T. M., D. J. Fornari, K. L. Von Damm, M. D. Lilley, R. M. Haymon, and R. A. Lutz, Temporal and spatial patterns of biological community development at nascent deep-sea hydrothermal vents along the East Pacific Rise, 9°49.6'N - 9°50.4'N, *Deep Sea Research,* Part II, *45,* 465-515, 1998.

Sinton, J. M., and R. S. Detrick, Mid-ocean ridge magma chambers, *J. Geophys. Res., 97,* 197-216, 1992.

Stevenson, J. M., and J. A. Hildebrand, Gravity modeling of a volcanically active site on the East Pacific Rise axis, *Tectonophysics, 254,* 57-68, 1996.

Stevenson, J. M., J. A. Hildebrand, and M. A. Zumberge, An ocean bottom gravity study of the southern Juan de Fuca Ridge, *J. Geophys. Res., 99,* 4875-4888, 1994.

Tivey, M. A., Vertical magnetic structure of the ocean crust determined from near-bottom magnetic field measurements, *J. Geophys. Res., 101,* 20,275-20,296, 1996.

Toomey, D. R., G. M. Purdy, S. C. Solomon, and W. Wilcox, The three dimensional seismic velocity structure of the East Pacific Rise near latitude 9°30'N, *Nature, 347,* 639-644, 1990.

Vera, E. E., and J. B. Diebold, Seismic imaging of layer 2A between 9°30'N and 10°N on the East Pacific Rise from two-ship wide-aperature profiles, *J. Geophys. Res., 99,* 3031-3041, 1994.

Von Damm, K. L., S. E. Oosting, R. Kozlowski, L. G. Buttermore, D. C. Colodner, H. N. Edmonds, J. M. Edmond, and J. M. Grebmeier, Evolution of East Pacific Rise hydrothermal vent fluids following a volcanic eruption, *Nature, 375,* 47-50, 1995.

Wang, X., J. R. Cochran, and G. A. Barth, Gravity anomalies, crustal thickness, and the pattern of mantle flow at the fast spreading East Pacific Rise, 9°-10°N: Evidence for three-dimensional upwelling, *J. Geophys Res., 101,* 17,927-17,940, 1996.

Warren, N., and B. R. Rosendahl, Velocity-density systematics for basalts drilled on the East Pacific Rise and Galapagos Rift during Deep-Sea Drilling Project Leg 54, *Initial Rep. Deep Sea Drill. Proj., 54,* 853-863, 1980.

Worzel, J. L., Continuous gravity measurements on a surface ship with the Graf sea gravimeter, *J. Geophys. Res., 64,* 1299-1315, 1959.

Wright, D. J., R. M. Haymon, and D. J. Fornari, Crustal fissuring and its relationship to magmatic and hydrothermal processes on the East Pacific Rise crest (9°12' to 54'N), *J. Geophys. Res., 100,* 6097-6120, 1995.

Zumberge, M. A., J. R. Ridgway, and J. A. Hildebrand, A towed marine gravity meter for near-bottom surveys, *Geophysics, 62,* 1386-1393, 1997.

B.J Coakley and J.R. Cochran, Lamont Doherty Earth Observatory of Columbia University, 109 Oceanography Building, P.O. Box 1000. RT 9W, Palisades, NY 10964. (jrc@ldeo.columbia.edu)

D.J. Fornari and M.A. Tivey, Department of Geology and Geophysics, Woods Hole Oceanographic Institution, Woods Hole, MA 02543.

R. Herr, Naval Oceanographic Office, Code N3113, Stennis Space Facility Center, MS 39522.

(Received March 10, 1998; revised January 14, 1999;
accepted January 25, 1999.)